R. & M. No. 3679

MINISTRY OF DEFENCE
AERONAUTICAL RESEARCH COUNCIL
REPORTS AND MEMORANDA

Free-Flight Measurements of Pressure and Heat Transfer on a Blunt Leading-Edge Caret Wing at Design and Off-Design Mach Numbers ($M_\infty = 0{\cdot}9$ to $3{\cdot}36$)

By G. H. GREENWOOD
Aerodynamics Dept., RAE, Farnborough

LONDON: HER MAJESTY'S STATIONERY OFFICE
1971
PRICE £1·61 NET

Free-Flight Measurements of Pressure and Heat Transfer on a Blunt Leading-Edge Caret Wing at Design and Off-Design Mach Numbers ($M_\infty = 0{\cdot}9$ to $3{\cdot}36$)

Aerodynamics Dept., RAE, Farnborough

Reports and Memoranda No. 3679*
July, 1970

Summary.

Pressure and heat-transfer measurements have been made in free flight on a caret wing with blunt leading edges and nose, at speeds below and above the design Mach number of 2·47. Comparison with data from a corresponding caret wing but with sharp leading edges indicates that the effect of blunting is confined to a region about 2 to 3 leading-edge diameters from the leading edge. At $M_\infty > 1{\cdot}5$ the data for the blunt leading edges and for the plane lifting surfaces were for the most part predicted with reasonable accuracy using easily-applied existing theory. A considerable reduction in heating rate was found in the wing junction.

*Replaces RAE Tech. Report 70129—A.R.C. 32 593.

1. *Introduction.*

In Ref. 1 measurements are presented of the kinetic heating and surface pressures relevant to a sharp-edged caret wing at design and off-design speeds—the design free-stream Mach number of the wing was 2·47. In this referenced test the heat-transfer data for the sharp wing were obtained in free flight and the surface pressure data from free flight and from wind tunnel tests using a scaled-down model of the free-flight wing.

In the present test, described herein, similar measurements were made entirely in free flight on a wing of the same basic geometry but having blunted leading edges and a tangent sphere nose, these modifications being a currently accepted palliative for the kinetic heating problem in practical aircraft applications.

The primary aim of the present test was to determine, by comparison with the sharp wing results from Ref. 1, the extent to which the surface pressures and heating were affected by the leading-edge and nose blunting.

At the same time the efficacy is assessed of easily-applied existing theory in predicting the surface pressures and heating rates appropriate to the lifting surfaces and leading edges of the blunt wing at both design and off-design speeds.

2. *Description of Test Head and Experimental Technique.*

The present wing had basically the same geometry as the sharp-edged caret wing of Ref. 1; both wings having a design Mach number of 2·47 and an incidence (i.e. slope of the ridge* line) of 12·13 degrees.

In the case of the present wing, however, the leading edges were rounded at 0·5 inch (12·7 mm) radius in a plane normal to the leading-edge sweep and the nose was blunted such that the geometric stagnation lines of the rounded leading edges were faired tangentially to a hemisphere of the same radius.

To provide an axisymmetric, non-lifting configuration suitable for free-flight testing a test head was compounded, in the same manner as for the wing in Ref. 1, from four compression surfaces of the present wing in the form of a 'Maikapar body'. The dimensions of the resulting test head are shown in Fig. 1 and a photograph in Fig. 2.

The method used to obtain heating data from free-flight models is described in Ref. 2. Briefly, the technique is to construct the wetted surfaces of the model from thin-gauge metal the heat capacity of which is known, and to calculate the heat transfer from the in-flight temperature/time history of the thin wall obtained from thermocouples welded to the inner surface. A wall of 0·036 inch (0·91 mm) gauge mild steel was used for the present test.

Heat-transfer measurements were made on the wing at the thermocouple locations shown in Fig. 20 and surface-pressure measurements were made on a different wing panel at the orifice locations shown in Fig. 5. The latter measurements were obtained from orifices drilled into the test-head surface and connected to model-borne telemetry transducers by copper pipes.

In-flight measurements from the thermocouples, pressure transducers and accelerometers (the latter were used to monitor any unwanted lift forces normal to the flight path) were telemetered to a ground station and recorded on magnetic tape for subsequent analysis.

The lower photograph of Fig. 2 illustrates the complete free-flight test vehicle as launched. This consists of the thin-walled test head followed by a conical fairing and a cylindrical telemetry bay which in turn is rigidly mounted in-line with the fin-stabilised solid-fuel rocket motor used to launch the complete assembly into a free-flight trajectory. Velocity and space coordinates during flight were obtained from range trackings using kinetheodolites, radar and radio-Doppler signals.

3. *Test Conditions.*

The maximum Mach number of the present test was 3·36. Table 1 lists the test conditions for the accelerating (i.e. heating) phase of the flight as values of Mach number, velocity, altitude, Reynolds number and the density, temperature and static pressure of the free stream. Only data for the accelerating phase of

*For consistency with Ref. 1 the term 'ridge' will be used hereafter to describe the line of intersection of the plane compression surfaces of the wing (see Fig. 1a).

the flight are presented in Table 1 because the determination of heat transfer becomes less accurate as zero-heat-transfer conditions are approached near maximum velocity.

4. *Flight Incidence Angle.*

The complete test vehicle (Fig. 2) was designed to fly at zero incidence (zero nett lift) to the free stream, but due to unavoidable built-in asymmetries in the component items (most particularly in the large stabilising fins) small lift forces were detected by the accelerometers. These are shown in Fig. 3 and are seen to be generally about 0·25 g. This acceleration relates to the complete test vehicle and in terms of flight incidence is judged to be small.

The flight incidence of the test head itself (which, because of elastic distortions, could differ from that of the complete test vehicle) was deduced from the data of Fig. 4 where the measured surface pressure from three of the ridge lines is compared with the theoretical two-dimensional wedge-flow pressures relevant to wedge angles one degree above and below the design ridge angle of 12·13 degrees. Fig. 4 indicates that for the most part the head incidence is less than one degree.

5. *Results.*

5.1. *Pressure Measurements.*

5.1.1. *Pressure at the nominal stagnation point on the model nose.* The primary purpose for making measurements of the nose stagnation pressure was to provide an independent source for checking the validity of the flight trajectory data obtained from the range observations (Section 2). This was done by comparing the measured stagnation pressure with the theoretical pressure downstream of a normal (nose) shock at the existing freestream Mach number and ambient static pressure.

This comparison is made in Fig. 6 and in general there is good agreement between experiment and theory—the small deviations representing at most about 0·6 per cent of the transducer range.*

The comparison in Fig. 6 is also a useful guide to the resolution of the telemetry process and of the subsequent recording and reduction procedures.

5.1.2. *Pressure on the leading-edge nominal stagnation line.* If there are no interference effects arising from the blunt nose, and if boundary-layer growth is ignored, the leading-edge pressure at zero incidence and for the present sweep angle (46 degrees) can be expected to be constant along the leading edge for any given Mach number. In the event, however, some pressure variations were measured along the leading edge as seen in Fig. 7 and 8.

Fig. 7 shows the variation with Mach number of the pressure at each of the six stations on the leading-edge nominal stagnation line compared with the two-dimensional theoretical[3] stagnation pressures calculated for the normal component, M_N, of the free-stream Mach number, M_∞, ($M_N = M_\infty \cos \Lambda$) assuming at $M_\infty \geqslant 1{\cdot}439$ (i.e. $M_N \geqslant 1{\cdot}0$) the presence of a detached normal shock at the leading edge. At two stations, P3 and P6, agreement with theory is good but elsewhere there are differences which are best seen in Fig. 8 which shows the variation in measured pressure along the leading edge for various Mach numbers. The manner of this variation would seem to discount nose interference effects and is more consistent with small differences in inclination between the orifices. For example, an orifice inclination of about one degree to the design leading-edge sweep angle would substantially account for the apparent pressure gradients along the leading edge.

If nose interference effects are present these are likely to be most discernible at the stations nearest the nose, i.e. at stations P1 and P2 (*see* Fig. 5). The pressures from these two stations are therefore compared in Fig. 9 where it is seen that the differences are small and probably represent little more than the experimental uncertainties. There is some indication, however, that at speeds below about $M_\infty = 2{\cdot}0$ the pressure at P2 is greater than that at P1, the reverse being true at higher speeds.

It is concluded, nevertheless, that if nose interference effects are present in the measurements of leading-edge pressure, they are small and within the experimental uncertainties.

---

*The transducer range at this station was 0–1379 k N m^{-2} abs. (0–200 lb in^{-2} abs.)

5.1.3. *Pressure distribution over the blunt leading edge.* Pressure measurements over the blunt leading edge were made at three angular stations, $\theta = 0$, 30 and 75·4 degrees where the angular coordinate, θ, is measured in a plane normal to the leading edge (Fig. 5). The pressure orifices themselves, however, were arranged in a plane normal to the ridge line (Fig. 5), but for consistency with other published data the measurements are referred to a plane normal to the leading edge as illustrated in Fig. 10.

Pressures at the above angular stations are presented for a range of Mach numbers in the upper frame of Fig. 11 in the normalised form C_p/C_{p_s} against angular coordinate θ, where C_p is the measured local pressure coefficient at $\theta = 30$ or 75·4 degrees and C_{p_s} is the measured coefficient at the stagnation point $\theta = 0$ degrees. The collapse of the data for $\theta = 30$ degrees shows that the normalised pressure at this angular station is virtually independent of free-stream Mach number for Mach numbers greater than about 1·5; the data for $\theta = 75{\cdot}4$ degrees have not been so effectively collapsed and indicate a substantial Mach number dependence and, for $M_\infty = 1{\cdot}0$, negative values of the pressure coefficient.

It is also clear from Fig. 11 that the modified Newtonian distribution $C_p/C_{p_s} = \cos^2\theta$ underestimates the bulk of the experimental data which are more closely represented by a $\cos^{3/2}\theta$ law. It should be noted, however, that the blunt leading-edge section is not a complete semicircle, the point of tangency to the flat surfaces of the wing being at $\theta = 75{\cdot}4$ degrees and the pressure at this station will therefore probably differ from that at a similar angular station on a complete semicircle (or cylinder) where the flow is allowed to expand freely.

The poor collapse of the data at $\theta = 75{\cdot}4$ degrees is, however, consistent with the observations of Ref. 4 where measurements of the surface pressures on hemispherically-blunt axisymmetric bodies (i.e. yaw meters) obtained from various sources are compared and are shown to have the common characteristic that at angular stations on the hemispherical nose having small inclinations to the stream direction (i.e. high values of θ) the pressure coefficients become progressively more negative as the free-stream Mach number is decreased. This results in an incomplete collapse of the data at these stations showing a substantial Mach number dependence of C_p/C_{p_s} at low supersonic speeds.

It was suggested in Ref. 4 that the use of the pressure coefficient in its conventional form, $C_p = (p-p_\infty)/q_\infty$, has no logical basis when applied to flows of the type existing behind a detached normal shock wave where the freestream ambient static pressure p_∞ is only indirectly of significance. It was found in Ref. 4 that the experimental pressures on a hemisphere were collapsed more successfully using a modified pressure coefficient $C_p{}^+ = (p-\frac{1}{2}p_\infty)/q_\infty$ and that the angular distribution of pressure on the hemisphere is best predicted by a derived empirical factor $\cos^n\theta$ ($\sin^n\psi$ in the nomenclature of Ref. 4) where n increases slowly from a value of 1·5 at low supersonic speeds to 2·3 at $M_\infty \to \infty$.

Because of the success in collapsing the three-dimensional flow measurements in Ref. 4 it was thought of interest to present the essentially two-dimensional leading-edge pressures of the present test in terms of the modified pressure coefficient $C_p{}^+ = (p-\frac{1}{2}p_\infty)/q_\infty$. This is done in the lower frame of Fig. 11 where it is seen that the new presentation has resulted in a somewhat better collapse of the data for Mach numbers above 1·5, particularly at the station $\theta = 75{\cdot}4$ degrees, and at both angular stations the low Mach number data ($M_\infty = 1{\cdot}0/1{\cdot}5$) have been more clearly delineated. The data are seen also to collapse best according to a $\cos^{1{\cdot}1}\theta$ law; distributions for $\cos^{3/2}\theta$ and $\cos\theta$ are shown for interest.

5.1.4. *Spanwise pressure distributions.* Spanwise distributions over the semi-wing are presented in Figs. 12, 13 and 14 for speeds below, near and above the design Mach number (2·47) respectively. The manner of presentation is as illustrated in Fig. 10, the data points being grouped in terms of their wetted distance, s, from the leading edge (non-dimensionalised in terms of the leading-edge radius, r) and projected on to a common plane normal to the leading edge.

Also shown in Figs. 12 to 14 are the two-dimensional wedge flow pressures[3] appropriate to a wedge of semi-angle equal to the wing design incidence of 12·13 degrees.

It is clear from Figs. 12 to 14 that the blunt leading edge has influenced the flow over a spanwise region of about two leading-edge diameters normal to the leading edge. The inboard extent of this region is evidently parallel to the leading edge and the region itself is characterised by a high pressure at the stagnation line, then a rapid decrease in pressure as the flow expands round the curved leading edge followed by a

re-compression to the flat surface value in the vicinity of two leading-edge diameters normal to the stagnation line (about three diameters streamwise).

A notable feature of the spanwise distributions in Figs. 12 to 14 is the generally good agreement between the wedge-flow values and the measured pressures on the flat surface ($s/r > 4$) inboard of the region of leading-edge interference both at the design and off-design speeds down to about $M_\infty = 1{\cdot}5$. Elsewhere there are some detailed deviations from theory, for example in the pressure distribution round the leading edge as noted in section 5.1.3. and Fig. 11, but the overall conclusion from the experimental results is that the surface pressure distribution over most of the lifting surface of the wing could be predicted closely enough for engineering purposes at least by easily-applied theory for speeds above $M_\infty = 1{\cdot}5$.

A possible exception to this conclusion is the pronounced pressure gradient in the chordwise direction (i.e. parallel to the ridge line) in the region of the aft pressure orifice array at longitudinal station 6. This is clearly revealed in Figs. 12 to 14 (black dot symbol) and more particularly so in the chordwise pressure distributions in Fig. 15.

This phenomenon occurs at all speeds from $M_\infty \approx 1{\cdot}5$ upwards and is sensitive to spanwise position, the highest gradient occurring at about mid-semispan at longitudinal station 6 (i.e. at orifice P22, Fig. 5) and diminishes towards the leading edge and at the ridge line. It will be seen (Section 5.2.2) that the heat transfer to the wing in this region, measured on a different wing surface, is also increased relative to the remainder of the flat surface.

No explanation can be offered for the occurrence of this local region of increased pressure and heating—the presence of the support fairing may be seen as a potential source of upstream interference but it should be noted (Fig. 1) that the slope of the fairing was designed to be continuous with the slope of the wing ridge line (12·13 degrees) and to present a backward-facing step at the wing/fairing junction. It should be further noted that no pressure gradient was measured along the ridge line (upper frame of Fig. 15) which would suggest no upstream interference effects in this region of the wing.

The spanwise pressure distributions at longitudinal stations 3 and 6 are shown in Fig. 16 normalised with respect to the leading-edge stagnation pressure in the form C_p/C_{p_s}. The higher mid-semispan pressures at longitudinal station 6 (upper frame of Fig. 16) compared with those at station 3 are clearly evident.

The distribution at longitudinal station 3 in Fig. 16 typifies the surface-pressure levels over most of the compression surface and shows that the pressure on the plane surfaces at the maximum test speed ($M_\infty = 3{\cdot}36$) is only about 20 per cent of the leading-edge stagnation pressure.

5.1.5. *Comparison with corresponding sharp wing.* Most of the surface pressure measurements for the corresponding sharp wing of Ref. 1 were in fact obtained from wind tunnel tests at $M_\infty = 1{\cdot}6$, 2·48 and 3·47 using a scaled model of the wing. Measurements in free flight were limited to three stations in the ridge lines and one on the wing flat surface.

These sharp-wing measurements, normalised with respect to theoretical wedge flow pressures[3], are compared with the present blunt-wing measurements in Figs. 17 and 19.

Because of the chordwise pressure gradient (Section 5.1.4.) and the consequently higher pressures at longitudinal station 6 compared with those for the remainder of the wing, the sharp/blunt wing comparison is made in two parts; Fig. 17 compares the spanwise pressure distributions for the sharp wing with those obtained from longitudinal station 3 on the blunt wing and Fig. 19 compares the sharp wing pressures with those from longitudinal station 6 on the blunt wing.

The comparisons of Fig. 17 show that there are large differences in the pressure levels of the sharp and blunt wings in the region near the leading edge ($\eta > 0{\cdot}4$) but at $M_\infty = 1{\cdot}6$ and 2·5 it is evident that blunting has not significantly affected the pressure level in the immediate region of the ridge ($\eta = 0$).

At $M_\infty = 3{\cdot}36/3{\cdot}47$, however, it is seen that the pressure ratio $C_p/C_{p_{\text{wedge}}}$ at $\eta = 0$ for the blunt wing does not significantly exceed unity whereas for the sharp wing the ratio $C_p/C_{p_{\text{wedge}}}$ is about 1·2. To emphasise this result, Fig. 18 shows the spanwise variation of $C_p/C_{p_{\text{wedge}}}$ at longitudinal station 3 on the blunt wing for a Mach number range 1·6 to 3·2. It is seen in Fig. 18 that at no time does the pressure in the ridge ($\eta = 0$) sensibly exceed the theoretical wedge pressure and is in fact only 4 per cent below the wedge value at $M_\infty = 1{\cdot}9$.

These results would seem to indicate that the leading-edge blunting has suppressed the trend towards pressures in excess of wedge flow values found [1,5] on sharp caret wings in the region of the ridge line ($\eta = 0$) at Mach numbers above the design value.

In the sharp/blunt wing comparisons of Fig. 19, using blunt wing data from longitudinal station 6, there is a marked increase in mid-semispan pressure for the blunt wing but at $M_\infty = 2{\cdot}5$ and 3·36/3·47, at least, the ridge line ($\eta = 0$) pressure is unaffected by blunting.

5.2. *Heat-Transfer Measurements.*

Only heat-transfer data obtained during the accelerating (heating) phase of the test are presented. This is because the determination of heat flow becomes less accurate as zero heat-transfer conditions are approached.

5.2.1. *Heat-transfer to leading-edge nominal stagnation line.* Fig. 21 shows the variation with freestream Mach number of the heat-transfer to the leading-edge nominal stagnation line. Theoretical values of the turbulent and laminar heat-transfer calculated by the methods of Ref. 6 are also shown.

It is seen that the experimental data are consistent with the existence of a transitional or a fully turbulent boundary layer at the stagnation line for all Mach numbers except for station F_2 (nearest functional thermocouple to the nose) where for speeds up to about $M_\infty = 1{\cdot}3$ the results are more consistent with a laminar boundary layer.

These results are consistent with the measurements of Ref. 6 inasmuch as turbulent stagnation heating was reported therein on a cylinder yawed 40 degrees. This latter result was obtained in a wind tunnel at $M_\infty = 4{\cdot}15$ and at a stream Reynolds number, based on cylinder diameter, of $3{\cdot}5 \times 10^6$ compared with $0{\cdot}4$ to $1{\cdot}7 \times 10^6$ for the present results.

Topham[7] has suggested that a suitable correlating parameter for the state of the swept stagnation-line boundary layer is the boundary-layer momentum-thickness Reynolds number, R_θ. Using experimental heating results from various sources Topham concludes that the critical R_θ for the onset of transitional stagnation-line flow is in the region of 130. In Fig. 22 the stagnation line heating results from the present test are plotted against R_θ; the experimental data (Q_E) are presented in terms of the theoretical[6] values for a laminar (Q_{lam}, Fig. 22a) and a turbulent (Q_{turb}, Fig. 22b) boundary layer. R_θ is appropriate to the spanwise flow component (i.e. parallel to the leading edge) and was calculated using the data presented in Refs. 7 and 10.

From Fig. 22a it is seen that the data below $R_\theta = 290$ are somewhat scattered but the trend suggests that the onset of transition (when Q_E/Q_{lam} exceeds unity) occurs at $R_\theta \approx 200$; this compares with $R_\theta \approx 130$ obtained in Ref. 7*.

Fig. 22b indicates that a fully turbulent boundary layer (when Q_E/Q_{turb} becomes unity) is obtained for R_θ in the region of 400 to 500; for this condition Topham[7] suggests $R_\theta \approx 450$ based on the results from the yawed cylinder tests of Ref. 6 which are reproduced in Fig. 22b.

In Fig. 23 heat-transfer distributions along the leading-edge nominal stagnation line are shown for various Mach numbers. These distributions show a generally constant heat-transfer rate along the leading edge for a given Mach number and this suggests that no significant interference effects from the blunt nose are present.

5.2.2. *Spanwise heat-transfer distributions.* Spanwise distributions of heat-transfer rates are presented in Figs. 24, 25 and 26 for Mach numbers below, near and above the design value respectively. The manner of presentation is as illustrated in Fig. 10.

The spanwise distributions of heating rate follow qualitatively for the most part those of the surface pressures shown in Figs. 12 to 14. In the leading-edge stagnation region the heating rates are a maximum

---

*The correlating parameters in the comparison with laminar theory in Ref. 7 were slightly different from those of the present test, being $(Q/Q_{\Lambda=0})$ experiment $\doteqdot (Q/Q_{\Lambda=0})$ theory against R_θ. $Q_{\Lambda=0}$ refers to the stagnation-line heating at zero sweep.

and they fall rapidly in magnitude over the leading-edge curvature and, by extrapolating the curved and flat surface data, would appear to reach a minimum level in the region of $s/r = 2$ to 3. At greater values of s/r the heating rates are seen to rise to an almost constant level over the semispan except for a marked decrease in the ridge line as indicated by the ringed data points.

This reduced heating rate in the ridge-line region is entirely consistent with published experimental results for corner flows (Ref. 8, for example) which show, as well as reduced heating rates in the corner, the existence of a region of peak heating associated with vortical flow near the corner. In the present test the spanwise spacing of the thermocouples was almost certainly too great to detect this peak heating region even if present.

Another notable feature about the spanwise heating distributions is the pronounced increase in heating on the flat surface of the wing at longitudinal station 6 compared with the other stations. This is seen in the distribution of the black dot symbol in Figs. 24 to 26 and reflects the higher surface-pressures measured at this longitudinal station (*see* Section 5.1.4. and Figs. 12 to 14); it is emphasised that this result was obtained from pressure and heating measurements made on different wing surfaces (*see* Figs. 5 and 20).

The spanwise heat-transfer rates at longitudinal stations 3 and 6 are shown in Fig. 27 normalized with respect to the leading-edge stagnation line heating. It is seen that the heat-transfer rate over the flat surfaces is only about 0·6 and in the ridge line only about 0·4 of that to the leading-edge stagnation line. Unlike the comparable pressure distributions at these stations (Fig. 16) the normalized values of heat transfer show little dependence on freestream Mach number.

In Figs. 28, 29 and 30 the experimental spanwise heat transfer (Q_E) to the flat surfaces of the semi-wing is compared with estimated* flat plate values appropriate to a turbulent boundary layer (Q_T) for freestream Mach numbers below, near and above the design value respectively. This presentation shows that the applied method[9] has predicted the heat-transfer rates over most of the semi-span with reasonable accuracy; the notable exceptions being in the region extending about two leading-edge diameters from the leading edge ($s/r \approx 4$) and in the ridge line (ringed data) where, at most speeds, the applied theory has over-estimated the heating rate by about 100 per cent.

5.2.3. *Comparison with corresponding sharp wing.* Spanwise distributions of the heat transfer to the corresponding sharp wing, taken entirely from the free-flight test of Ref. 1, are compared for various Mach numbers with the present blunt wing data in Fig. 31.

The quantity compared in Fig. 31 is Q_E, the measured heat-transfer rate to the wing surface; direct comparison of this quantity is possible between the two tests because the thickness and thermal properties of the wing materials were identical.

The most notable feature in the comparisons of Fig. 31 is that the heat-transfer to the inboard part of the wing ($\eta <$ about 0·5) has not been significantly affected by the leading-edge blunting.

6. *Conclusions and Observations.*

Pressure and heat-transfer measurements have been made in free-flight at Mach numbers up to 3·36 on a blunt-leading-edge caret wing of design Mach number 2·47, incidence 12·13 degrees and leading-edge sweep 46 degrees. These measurements, together with comparisons with similar measurements made on a corresponding sharp wing, have led to the following conclusions and observations:

(1) The blunt leading edge directly affected the surface pressures and heat transfer for a distance of 2 to 3 leading-edge diameters normal to the leading edge (3 to 4 diameters streamwise), the region of interference being parallel to the leading edge.

(2) The pressures over the blunt leading edge were somewhat under-estimated by modified Newtonian theory, $C_p = C_{p_s} \cos^2 \theta$, the distribution being more in accord with a $\cos^{3/2} \theta$ law. The use of a modified[4]

*Based on Ref. 9 using measured values of local pressure and temperature; the resulting estimated local heat transfer is appropriate to an isothermal wedge of 12·13 degrees semi-angle (i.e. the design incidence of the test wing) with an attached shock and a turbulent boundary layer. An emissivity factor of 0·76 and a turbulent recovery factor of 0·89 were assumed in the calculations.

pressure coefficient, $C_p{}^+ = (p - \frac{1}{2} p_\infty)/q_\infty$ together with a derived distribution factor $\cos^{1\cdot1} \theta$ provided the better collapse of the leading-edge pressures. This conclusion is qualified by the fact that the measurement station at $\theta = 75{\cdot}4$ degrees is located at the point of tangency between the curved and plane wing surfaces, i.e. in a region of over-expanded flow.

(3) There is some evidence that the high inboard surface pressures measured in published tests (e.g. Refs. 1 and 5) on sharp-edged caret wings at Mach numbers above the design value have been suppressed by leading-edge blunting of the present magnitude. On the present blunt wing the inboard pressures in the region of the ridge were always within about 4 per cent of the two-dimensional wedge flow values over a speed range $1{\cdot}9 \leqslant M_\infty \leqslant 3{\cdot}36$.

(4) At Mach numbers from about 1·5 upwards the pressures over most of the lifting surface of the wing, including the leading-edge stagnation pressures, were predicted with reasonable accuracy by easily-applied theory[3]. An exception, however, was the region of high pressure, found at about mid-semispan towards the rear of the wing, which was underestimated by about 20 to 30 per cent by two-dimensional wedge flow theory.

(5) At Mach numbers from about 1·5 upwards the heat-transfer rates to the lifting surface of the wing (other than to the ridge line and the region influenced by the blunt leading edge) were predicted with reasonable accuracy by theoretical flat-plate, turbulent flow values based on the methods of Ref. 9. The heating rates in the region of the ridge line were, however, at most speeds, between 50 and 60 per cent of the values predicted by this method.

(6) For the most part the local heat-transfer rate reflected qualitatively the local surface pressure; when the latter was high the heating rate was high, the converse being also true. (It should be noted that different wing surfaces were used for the heating and pressure measurements.)

(7) The magnitude of the heat transfer to the leading-edge nominal stagnation line was consistent with either a transitional or a fully turbulent boundary layer at all stations and at all Mach numbers from 1·0 to 3·36 (maximum speed of the test) with the exception of one station near the nose where the heating rate was consistent with a laminar boundary layer at speeds up to about $M_\infty = 1{\cdot}3$ and a turbulent or transitional boundary layer thereafter.

(8) A tentative correlation of the heat-transfer to the leading edge in terms of the boundary-layer momentum thickness Reynolds number, R_θ, in the manner of Ref. 7, shows that the critical R_θ for the onset of stagnation-line boundary-layer transition (i.e. when the kinetic heating exceeds laminar theory[6]) is about 200 and that the stagnation-line flow is fully turbulent (i.e. the kinetic heating is consistent with turbulent theory[6]) for $R_\theta \approx 400$ to 500.

(9) There is no evidence from either the pressure or heat-transfer measurements to suggest that interference effects attributable to the blunt nose were present.

LIST OF SYMBOLS

C_p Pressure coefficient, $(p-p_\infty)\,q_\infty^{-1}$

C_p^+ Modified pressure coefficient, $(p-\frac{1}{2}p_\infty)\,q_\infty^{-1}$

F Refers to a fast-sampled (80 Hz) thermocouple station

M Mach number

P Static pressure; or, when used with numerical subscript, refers to pressure-measurement station

Q Heat-transfer rate

q Kinetic pressure

R_θ Reynolds number based on boundary-layer momentum thickness

r Radius of blunt leading edge

S Refers to a slow-sampled (3·3 Hz) thermocouple station

s Spanwise dimension along wetted surface of wing normal to the leading edge

η Fraction of semispan of the corresponding sharp-edged wing

θ Angular coordinate appropriate to the blunt leading edge

Λ Leading-edge sweep angle at the wing design incidence

Subscripts

E Experimental quantity

N Normal to leading edge

s Stagnation conditions

T Theoretical quantity

∞ Free-stream conditions

REFERENCES

No.	*Author(s)*	*Title, etc.*
1	J. Picken and G. H. Greenwood	Free-flight measurements of heat transfer and observations of transition on a caret wing at Mach numbers up to 3·6. R.A.E. Technical Report 65237 (A.R.C. 27820) (1965)
2	J. Picken and D. Walker	Techniques for the investigation of aerodynamic-heating effects in free flight. AGARD Report 376 (1961) R.A.E. Technical Note Aero 2758 (A.R.C. 23125) (1961)
3	Ames Research Staff	Equations, tables, and charts for compressible flow. NACA Report 1135 (1953)
4	L. J. Beecham	The hemispherical, differential pressure yaw-meter at supersonic speed. A.R.C., R. & M. 3237 (1960)
5	L. F. Crabtree and D. A. Treadgold	Experiments on hypersonic lifting bodies. R.A.E. Technical Report 67004 (A.R.C. 29192) (1967)
6	I. E. Beckwith and J. J. Gallagher	Local heat transfer and recovery temperatures on a yawed cylinder at a Mach number of 4·15 and high Reynolds numbers. NASA Technical Report R-104 (1961)
7	D. R. Topham	A correlation of leading-edge transition and heat transfer on swept cylinders in supersonic flow. Hawker Siddeley Aviation; Report APG/2038/15 (A.R.C. 26219) (1964)
8	P. C. Stainback and L. M. Weinstein	Aerodynamic heating in the vicinity of corners at hypersonic speeds. NASA TN-D-4130 (1967)
9	L. F. Crabtree, R. L. Dommett and J. G. Woodley	Estimation of heat transfer to flat plates, cones and blunt bodies. A.R.C. R. & M. 3637 (1965)
10	E. Reshotko and I. E. Beckwith	Compressible laminar boundary layer over a yawed infinite cylinder with heat transfer and arbitrary Prandtl number. NASA Report 1379 (1958)

TABLE 1

Trajectory Data for Accelerating (Heating) Flight

Flight time from launch (s)	Mach number	Velocity ($m\ s^{-1}$)	Altitude (m)	Air density ($kg\ m^{-3}$)	Air temperature (°K)	Reynolds number per metre $\times 10^{-6}$	Static pressure ($kN\ m^{-2}$)
0·983	0·80	269	51	1·213	279·6	18·6	97·64
1·083	0·90	302	58	1·212	279·5	21·0	97·52
1·183	1·00	336	69	1·210	279·4	23·3	97·37
1·285	1·10	369	85	1·210	279·3	25·6	97·17
1·385	1·20	403	99	1·207	279·2	27·8	97·03
1·486	1·30	436	114	1·206	279·0	30·1	96·86
1·587	1·40	469	130	1·204	278·9	32·4	96·65
1·690	1·50	503	148	1·202	278·7	34·7	96·43
1·793	1·60	536	166	1·200	278·5	36·9	96·23
1·894	1·70	569	186	1·198	278·3	39·2	95·97
2·001	1·80	603	206	1·196	278·1	41·4	95·72
2·113	1·90	636	236	1·193	277·8	43·7	95·45
2·222	2·00	669	253	1·191	277·6	45·9	95·17
2·332	2·10	702	274	1·185	277·3	48·1	94·87
2·443	2·20	735	307	1·185	277·0	50·2	94·54
2·551	2·30	768	335	1·182	276·8	52·4	94·20
2·658	2·40	801	361	1·179	276·5	54·6	93·86
2·765	2·50	834	389	1·177	276·2	56·7	93·56
2·871	2·60	867	421	1·173	275·9	58·8	93·18
2·974	2·70	900	454	1·169	275·6	60·9	92·73
3·077	2·80	933	485	1·167	275·3	63·0	92·44
3·182	2·90	966	521	1·164	275·1	65·1	92·10
3·286	3·00	998	553	1·161	274·7	67·2	91·75
3·387	3·10	1031	585	1·157	274·4	69·3	91·38
3·491	3·20	1063	619	1·154	274·1	71·3	91·00
3·622	3·30	1096	661	1·149	273·6	73·3	90·50
3·800	3·36	1114	728	1·143	273·0	74·2	89·73

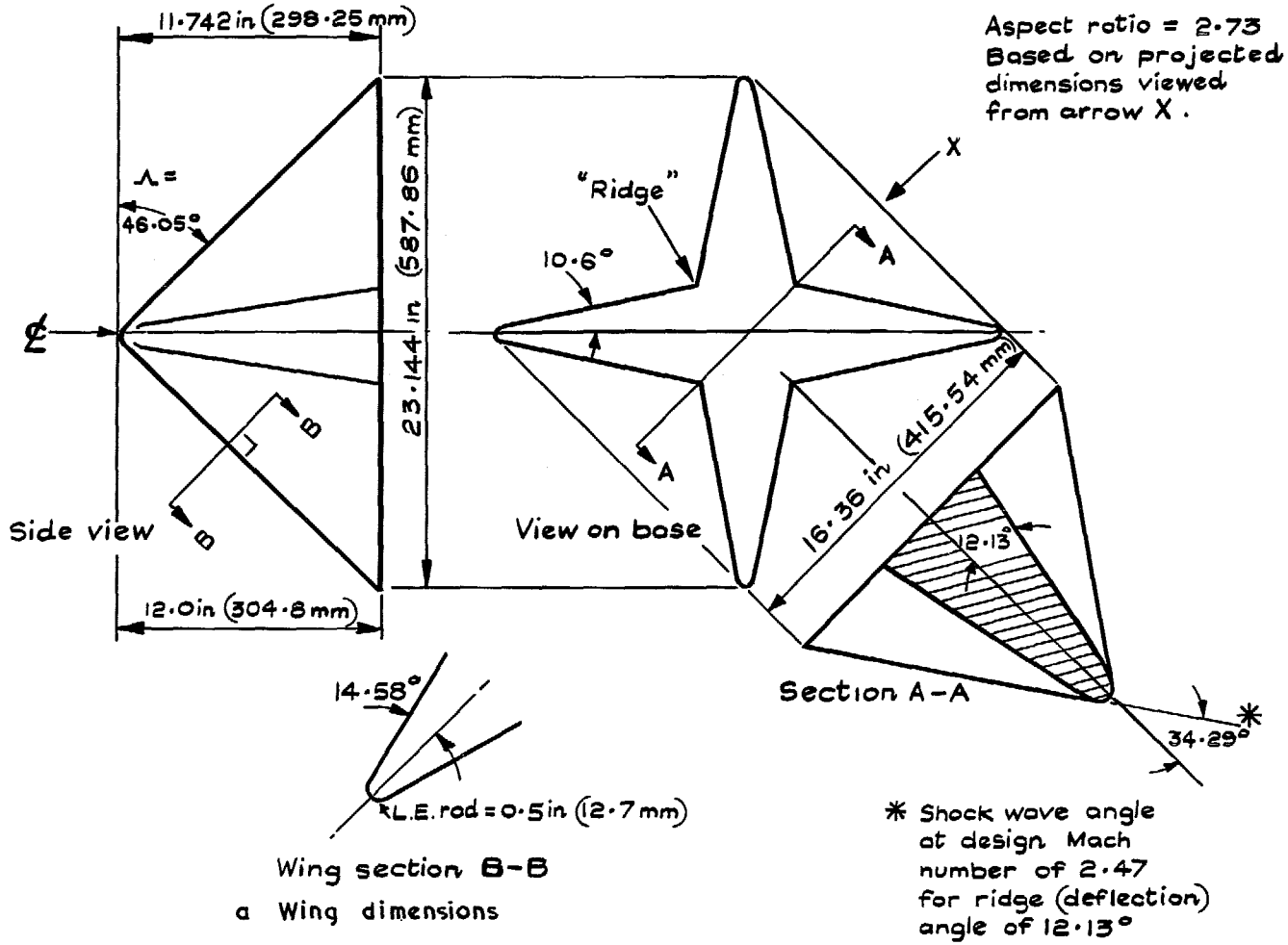

FIG. 1a. Geometry of test head.

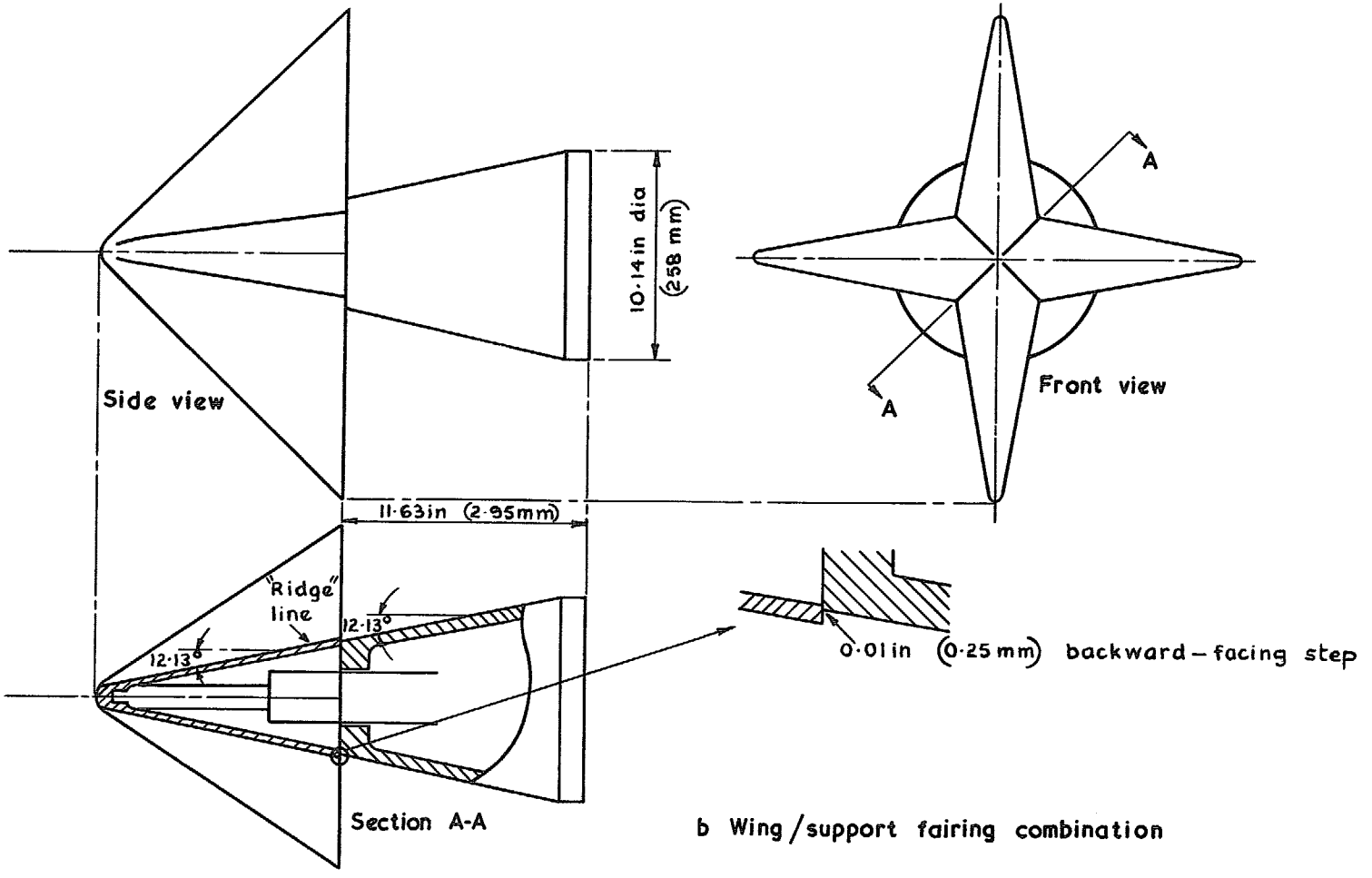

FIG. 1b. Geometry of test head.

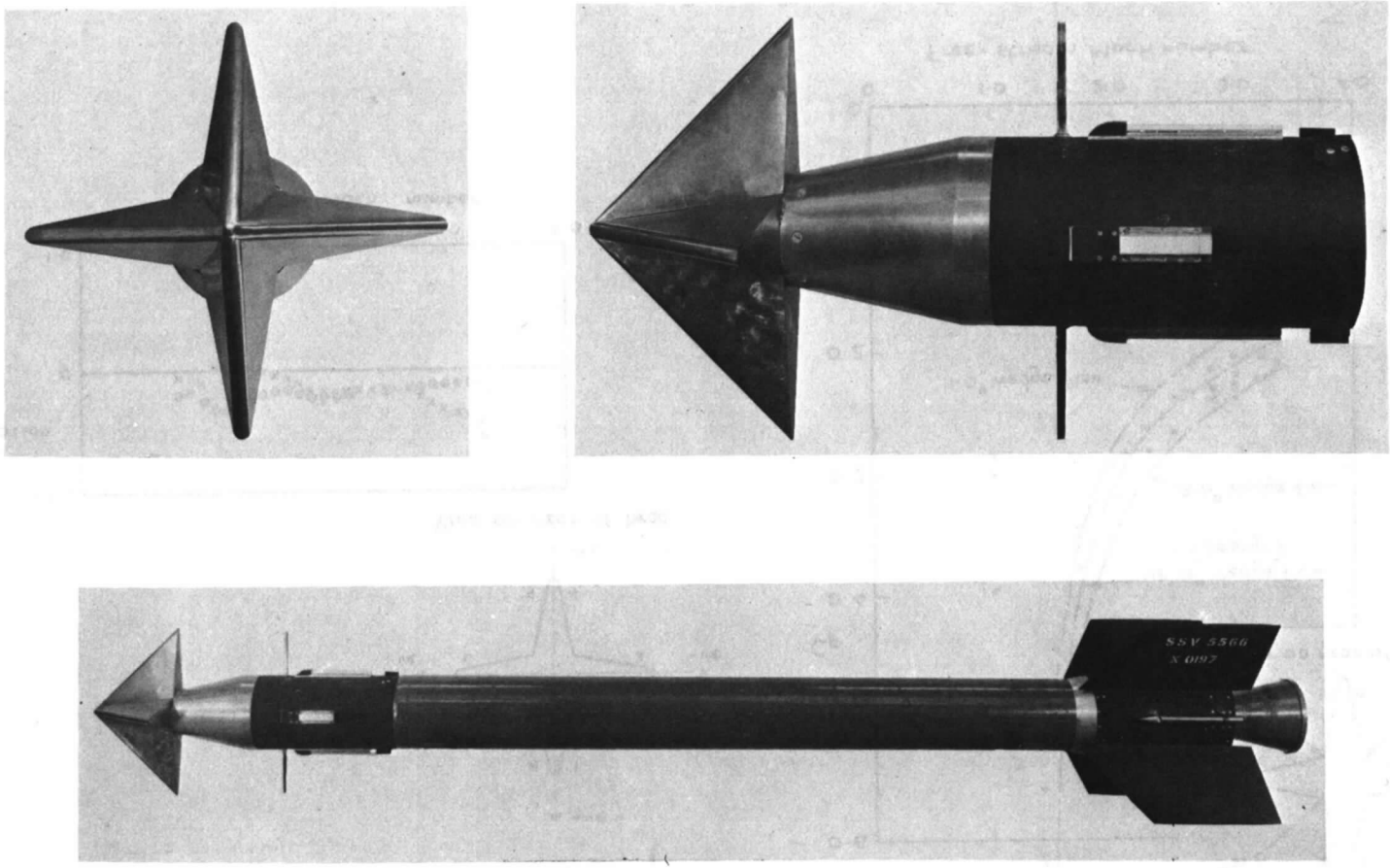

FIG. 2. Test head and boosting arrangement.

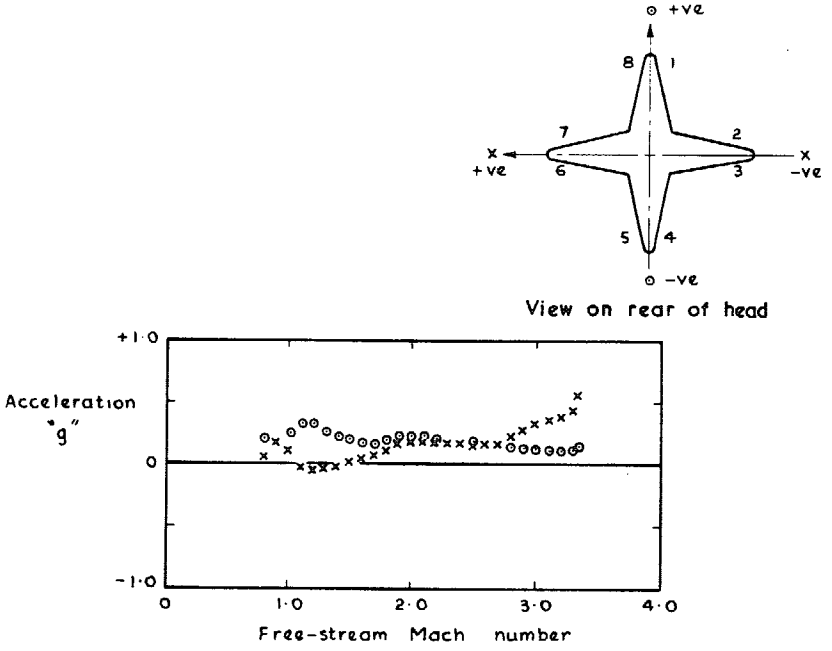

FIG. 3. Accelerations normal to head axis (accelerating flight).

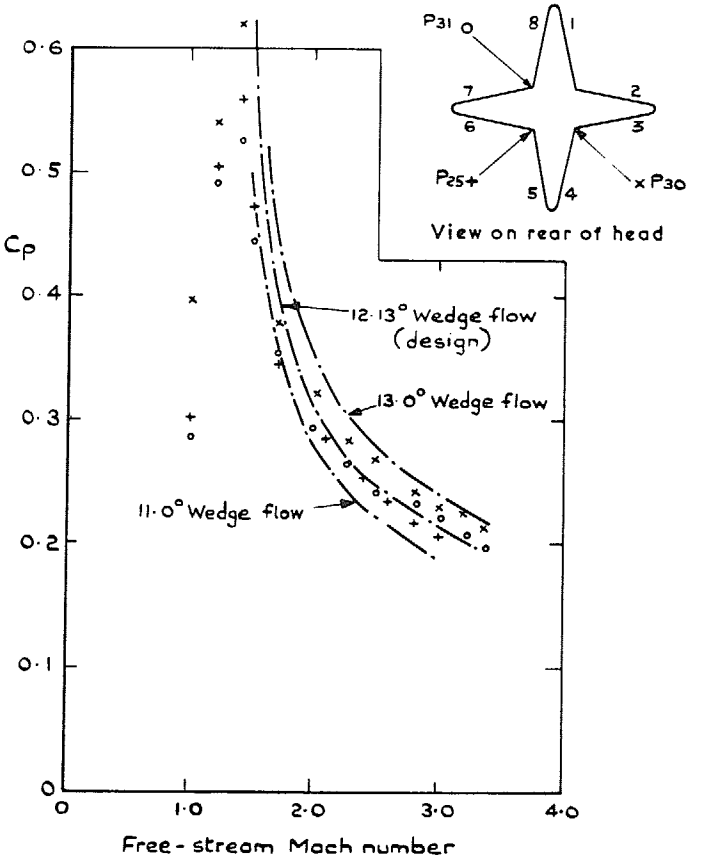

FIG. 4. Comparison of ridge-line pressures (accelerating flight).

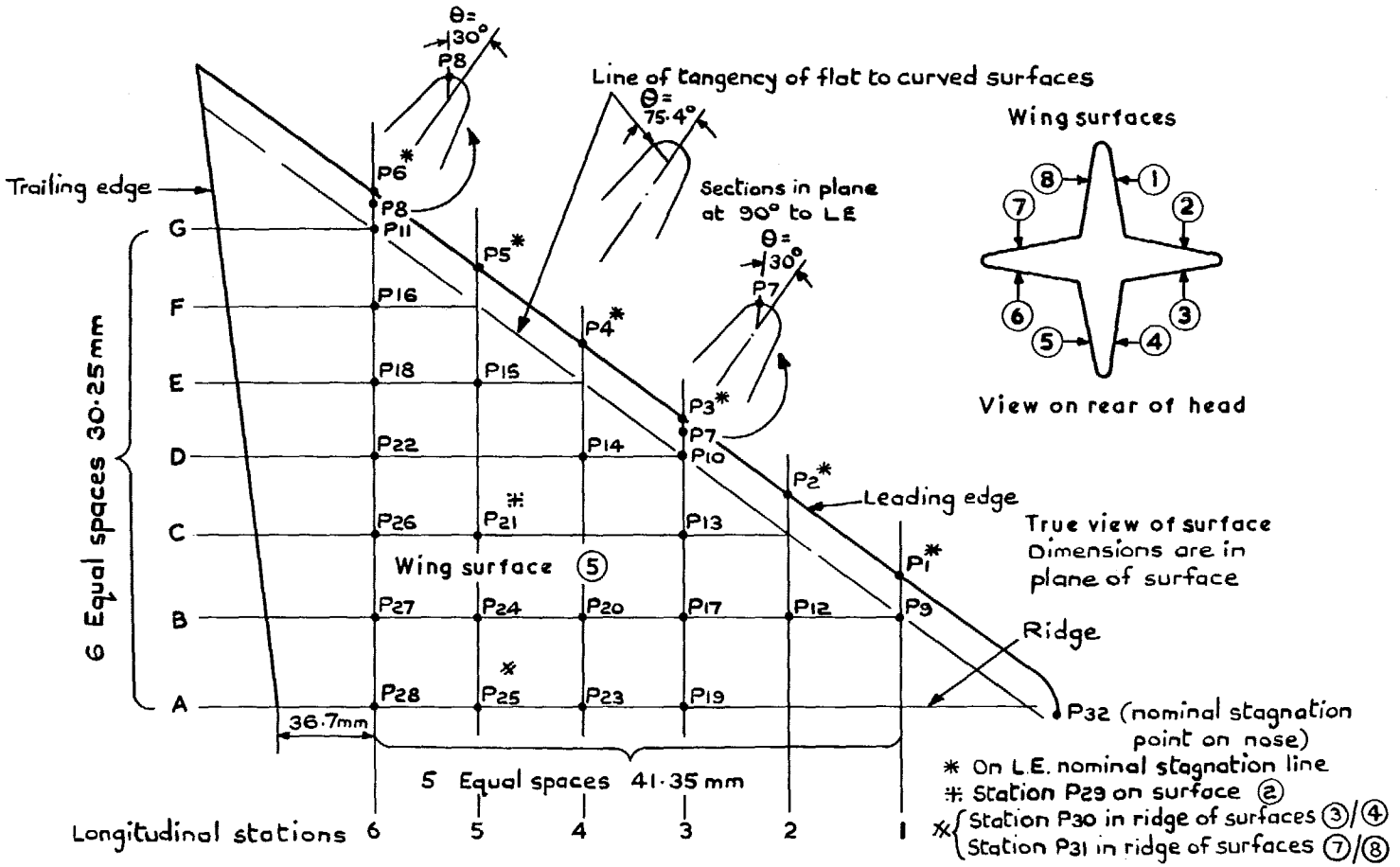

FIG. 5. Pressure orifice locations.

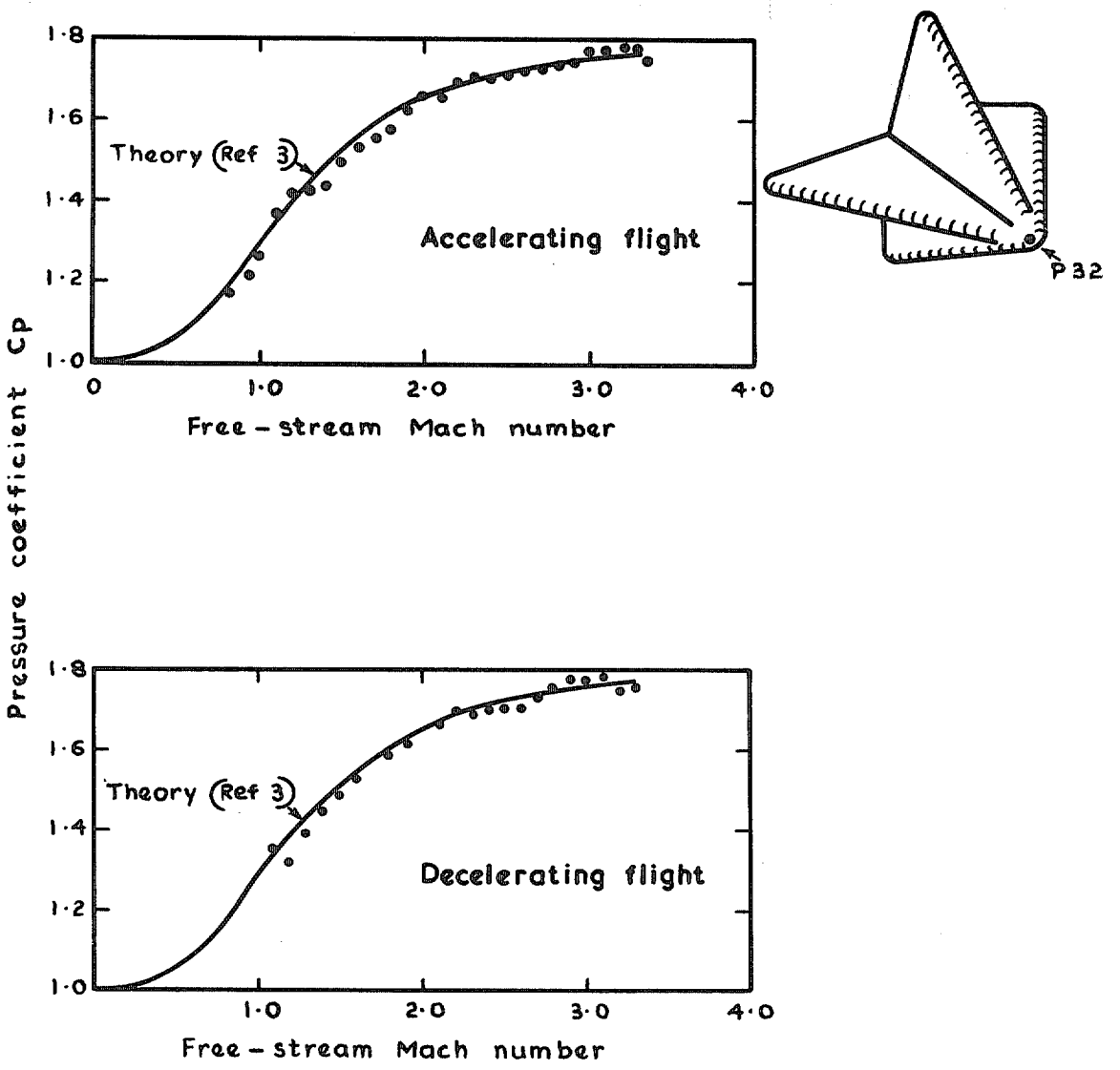

FIG. 6. Pressure at nominal stagnation point on nose.

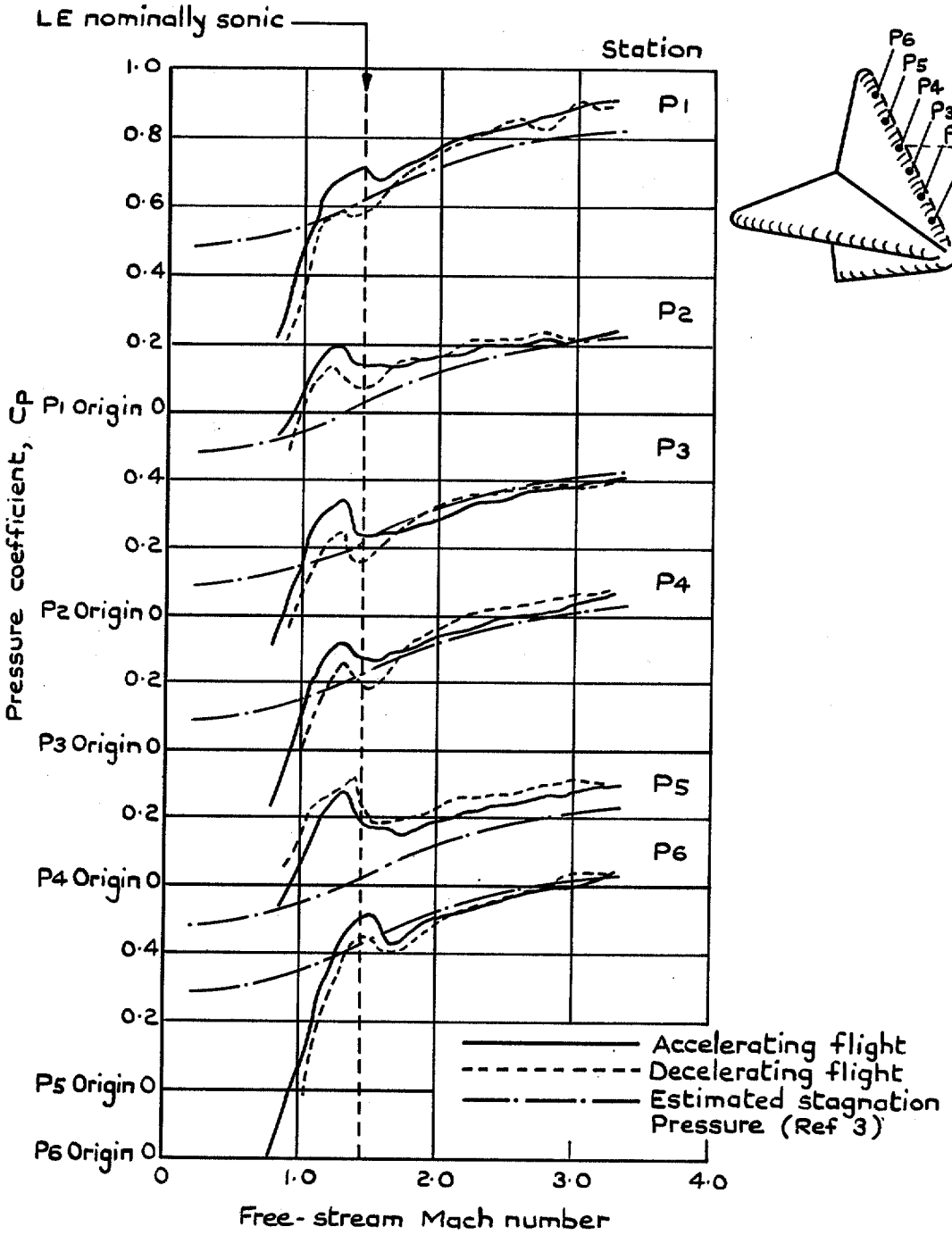

FIG. 7. Variation of leading-edge nominal stagnation pressure with free-stream Mach number.

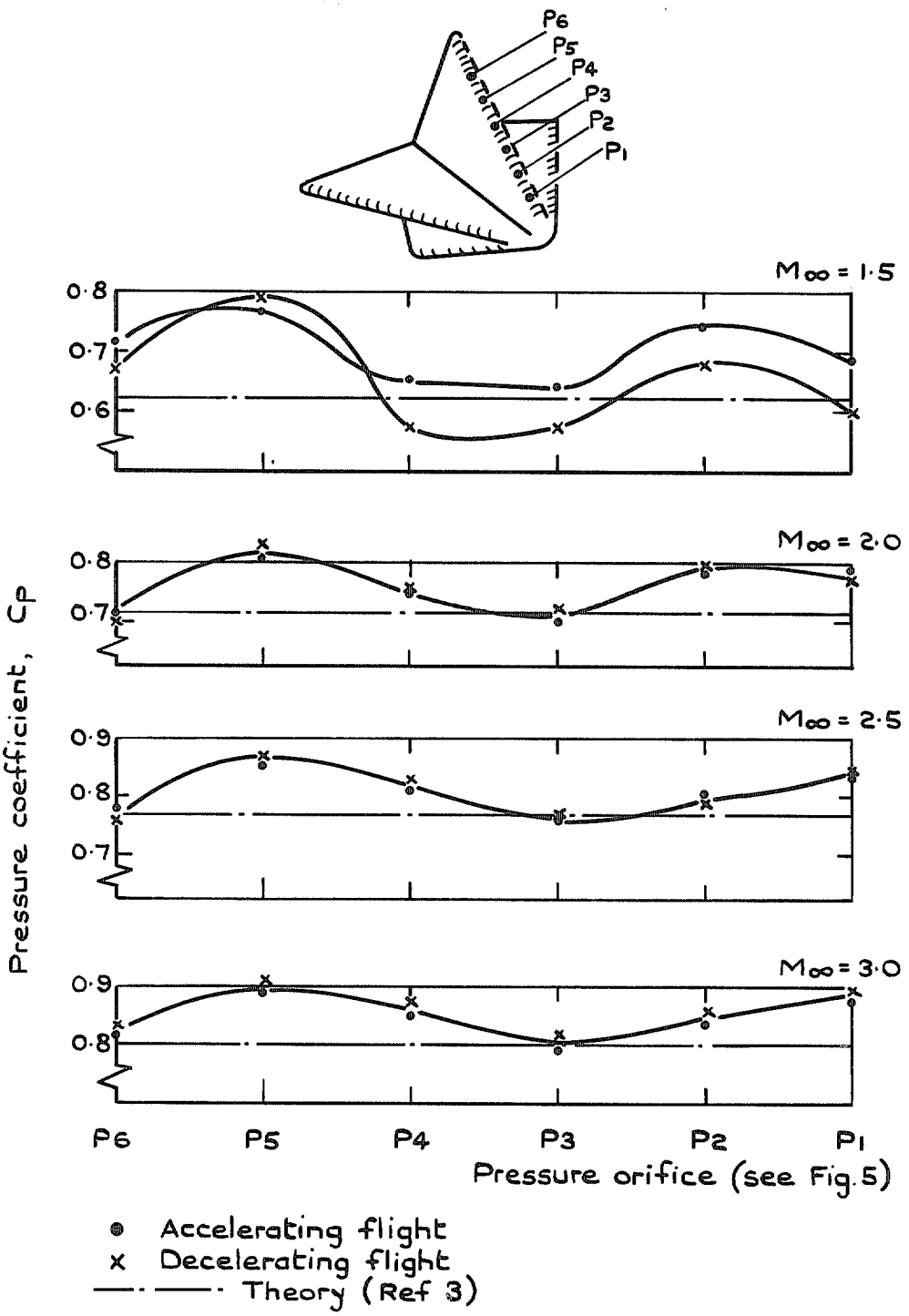

FIG. 8. Variation of pressure along leading-edge nominal stagnation line.

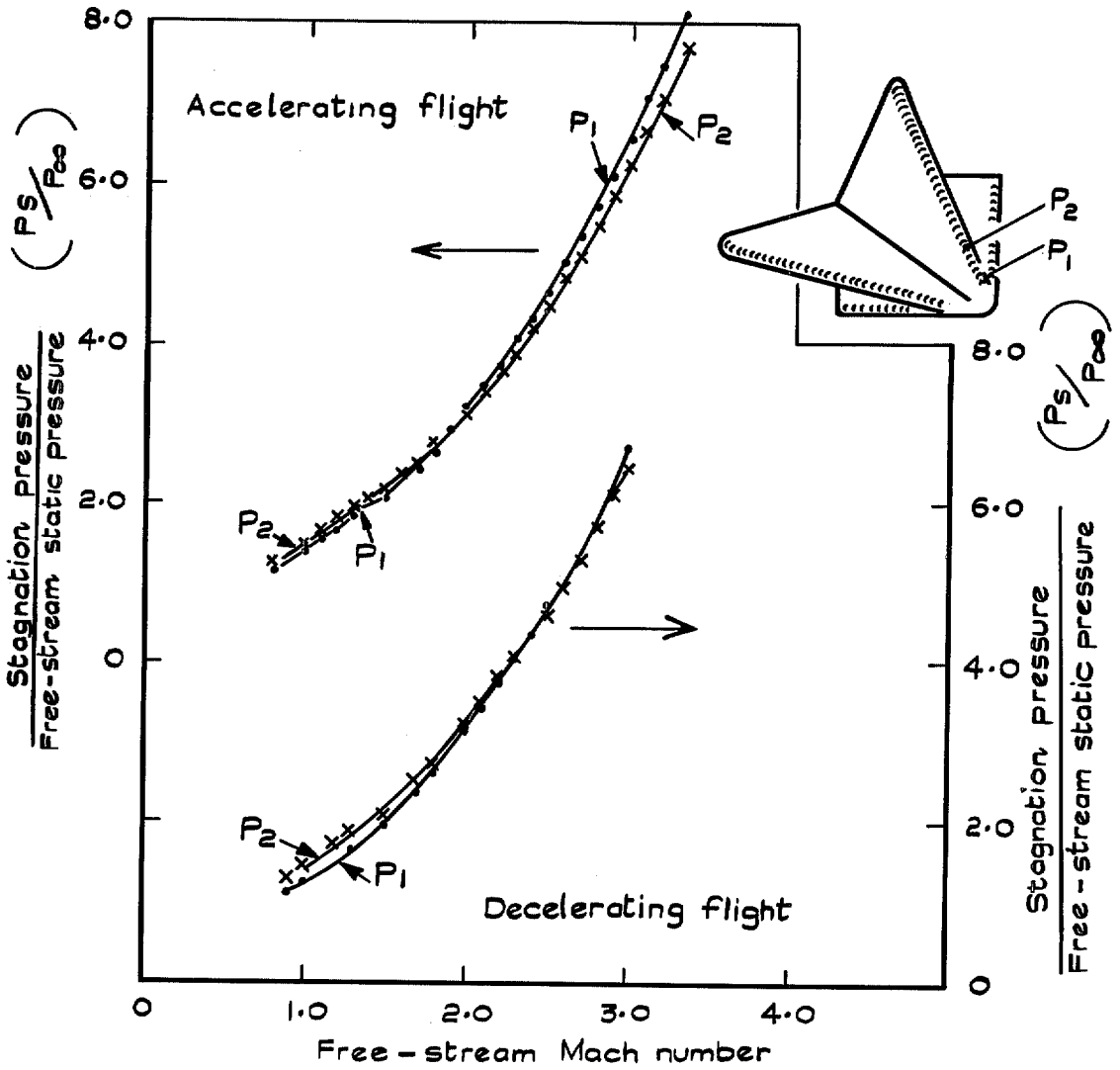

FIG. 9. Variation of leading-edge nominal stagnation pressure at stations P1 and P2 with free-stream Mach number.

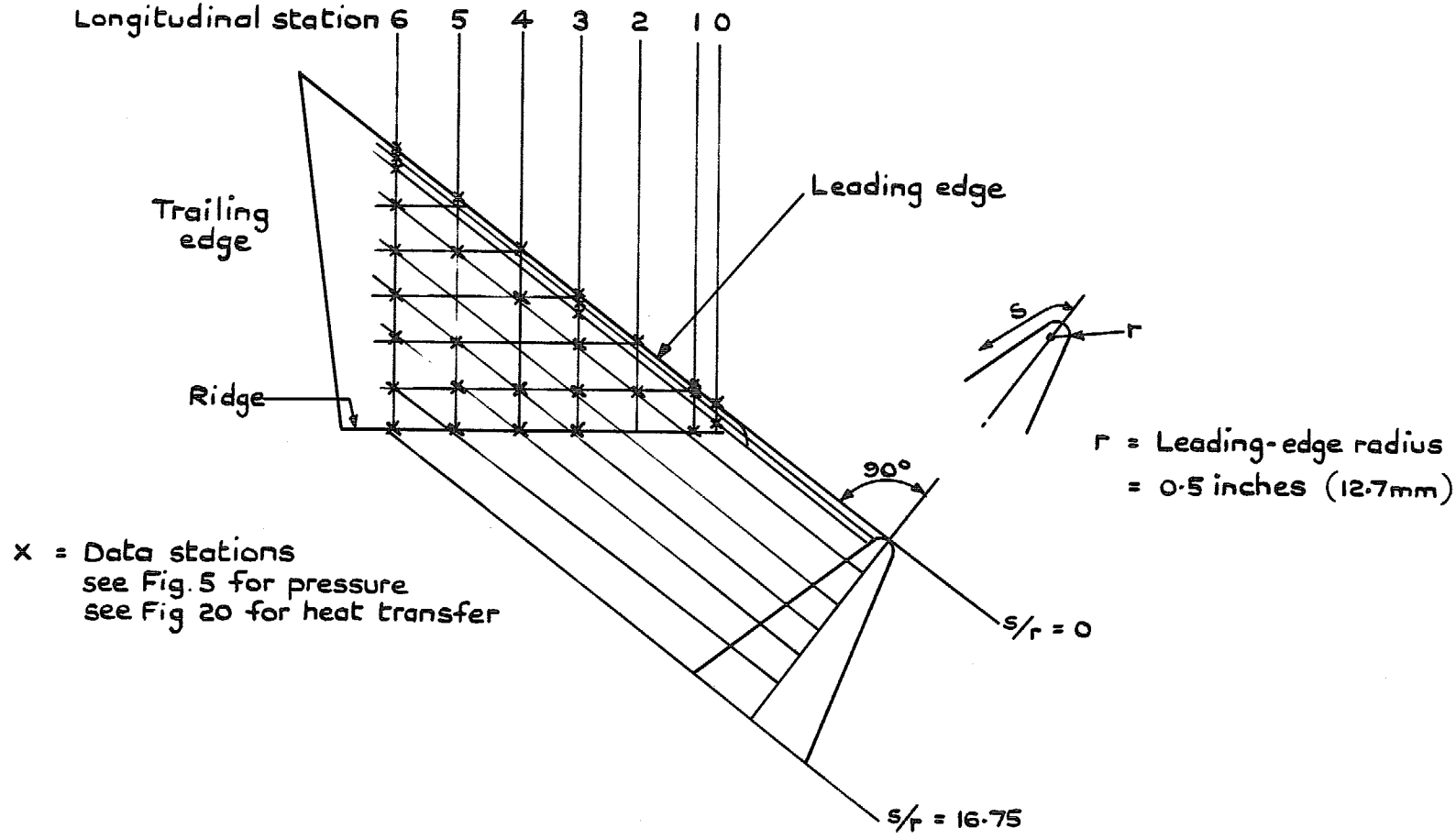

FIG. 10. Spanwise presentation of data.

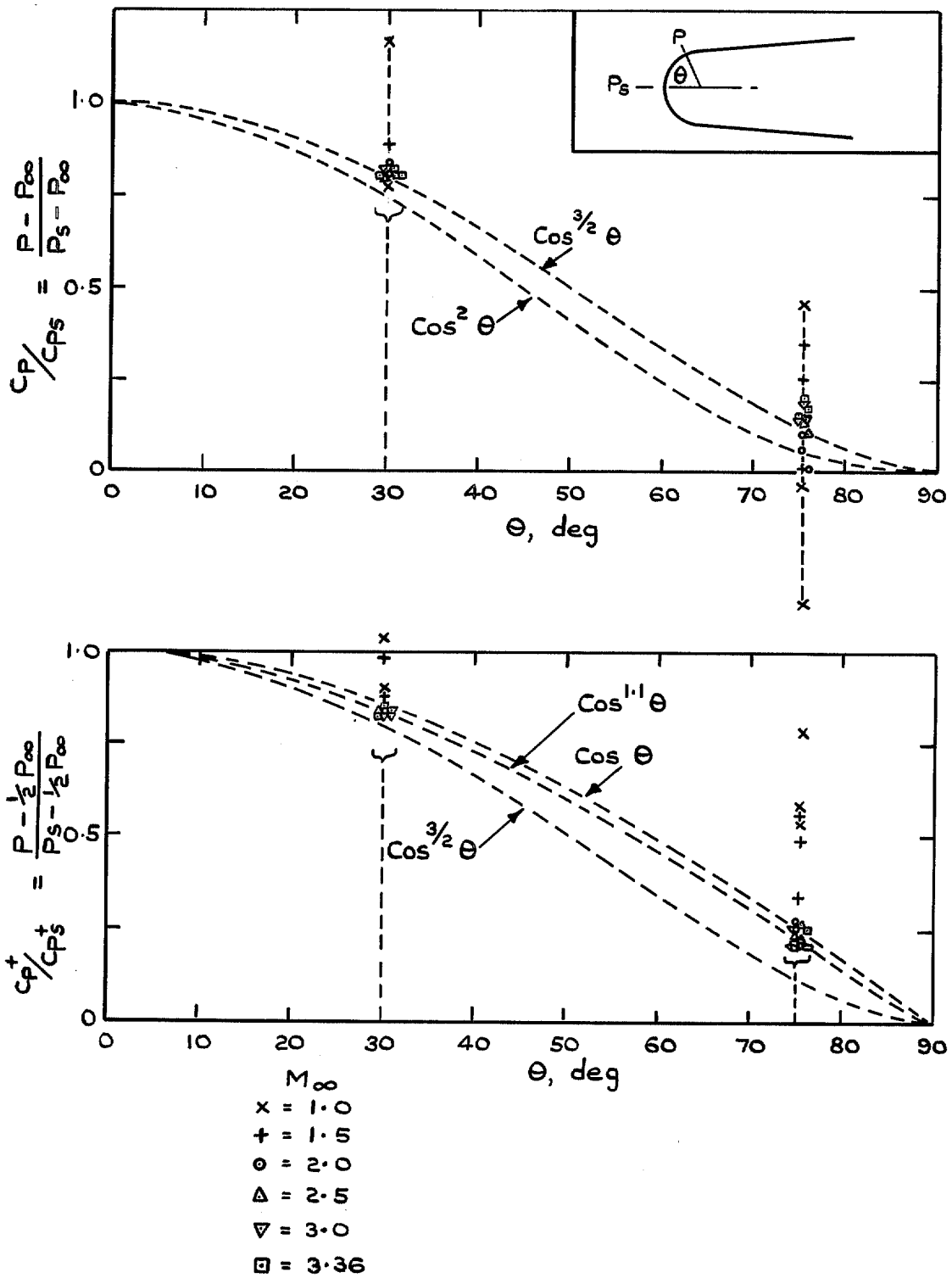

FIG. 11. Variation of C_p/C_{p_s} with angular station on leading edge.

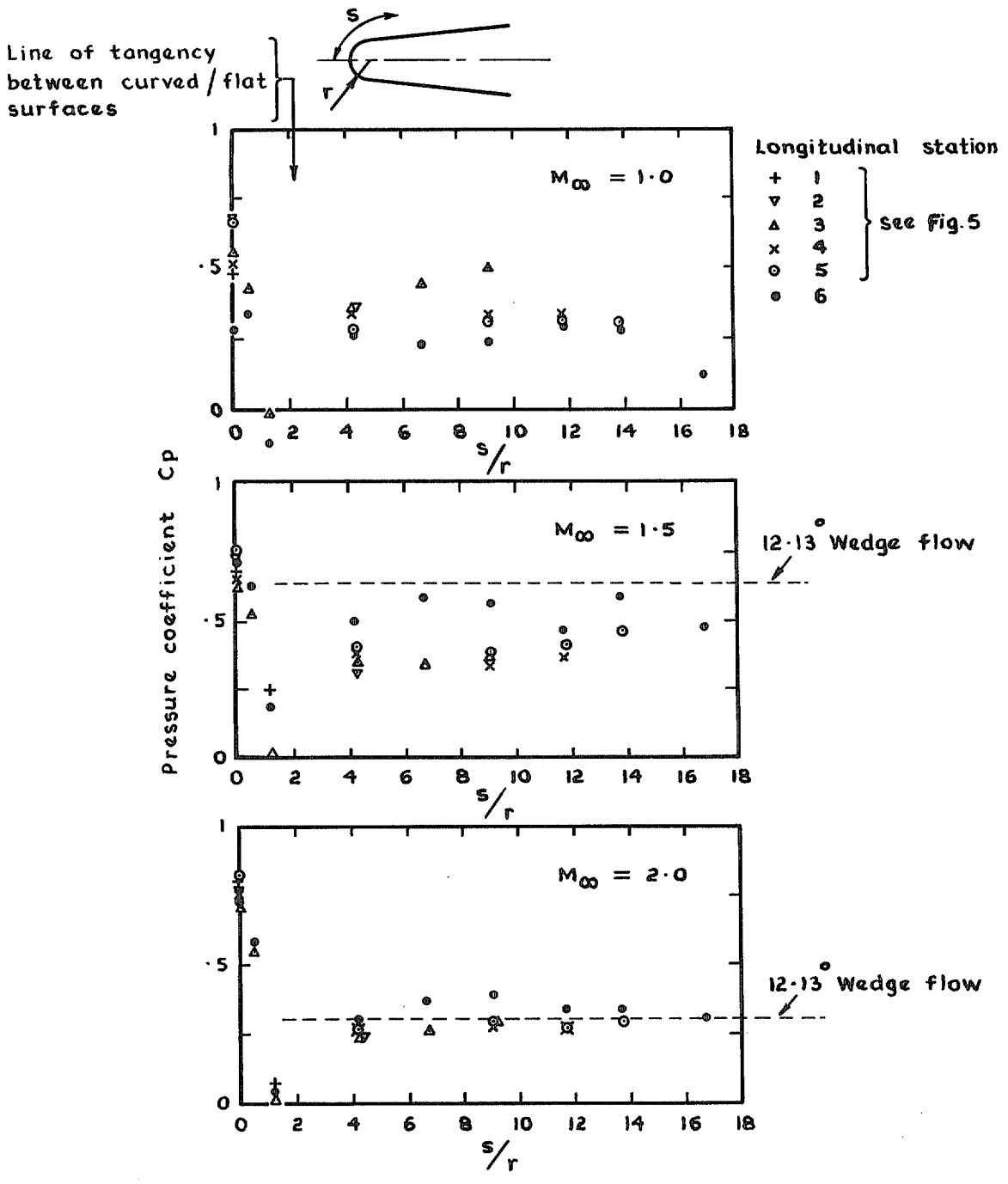

FIG. 12. Spanwise pressure distribution for M_∞ below design Mach number (i.e. $M_\infty < 2{\cdot}47$) (accelerating flight).

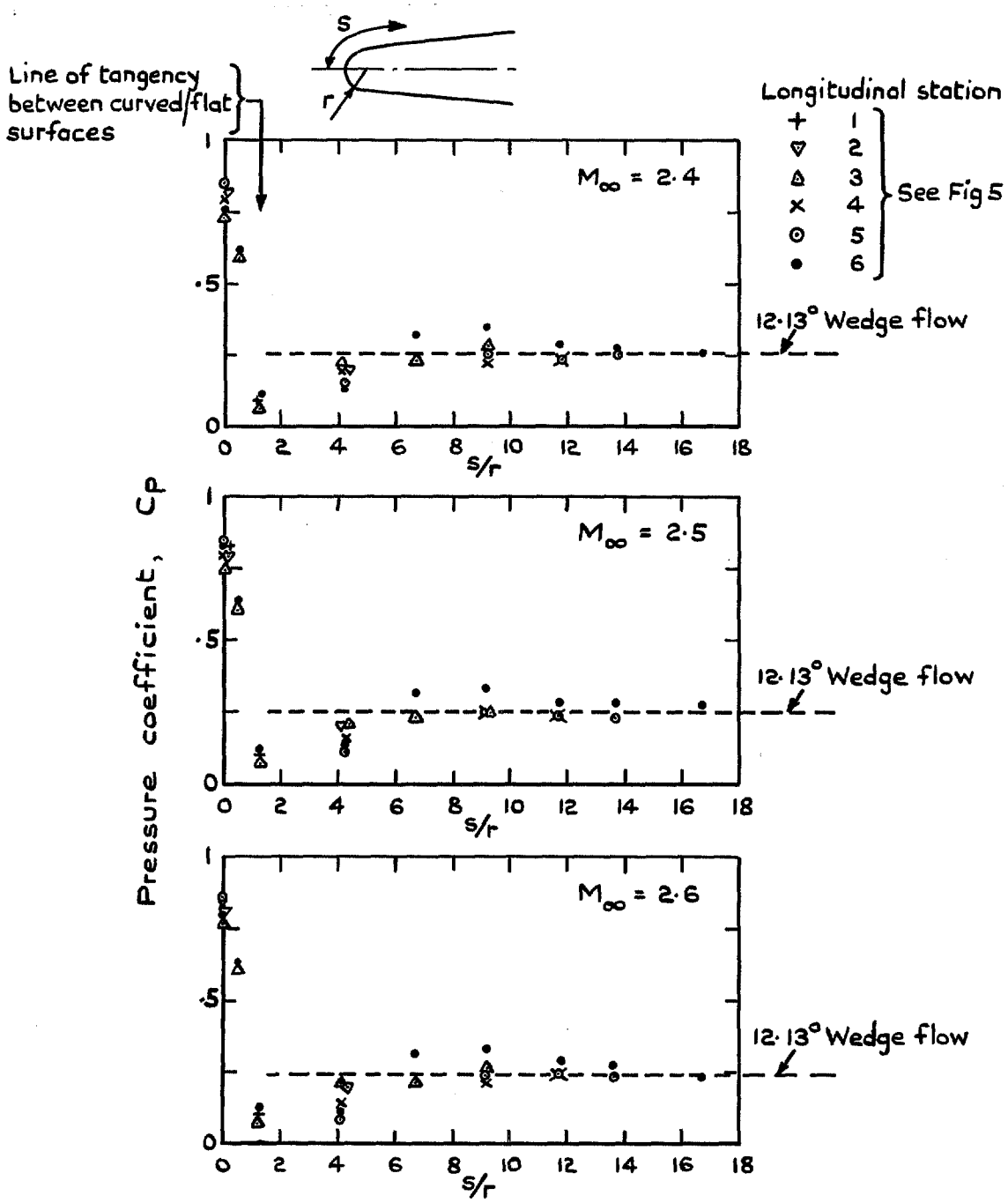

FIG. 13. Spanwise pressure distribution for M_∞ near design Mach number (i.e. $M_\infty \approx 2{\cdot}47$) (accelerating flight).

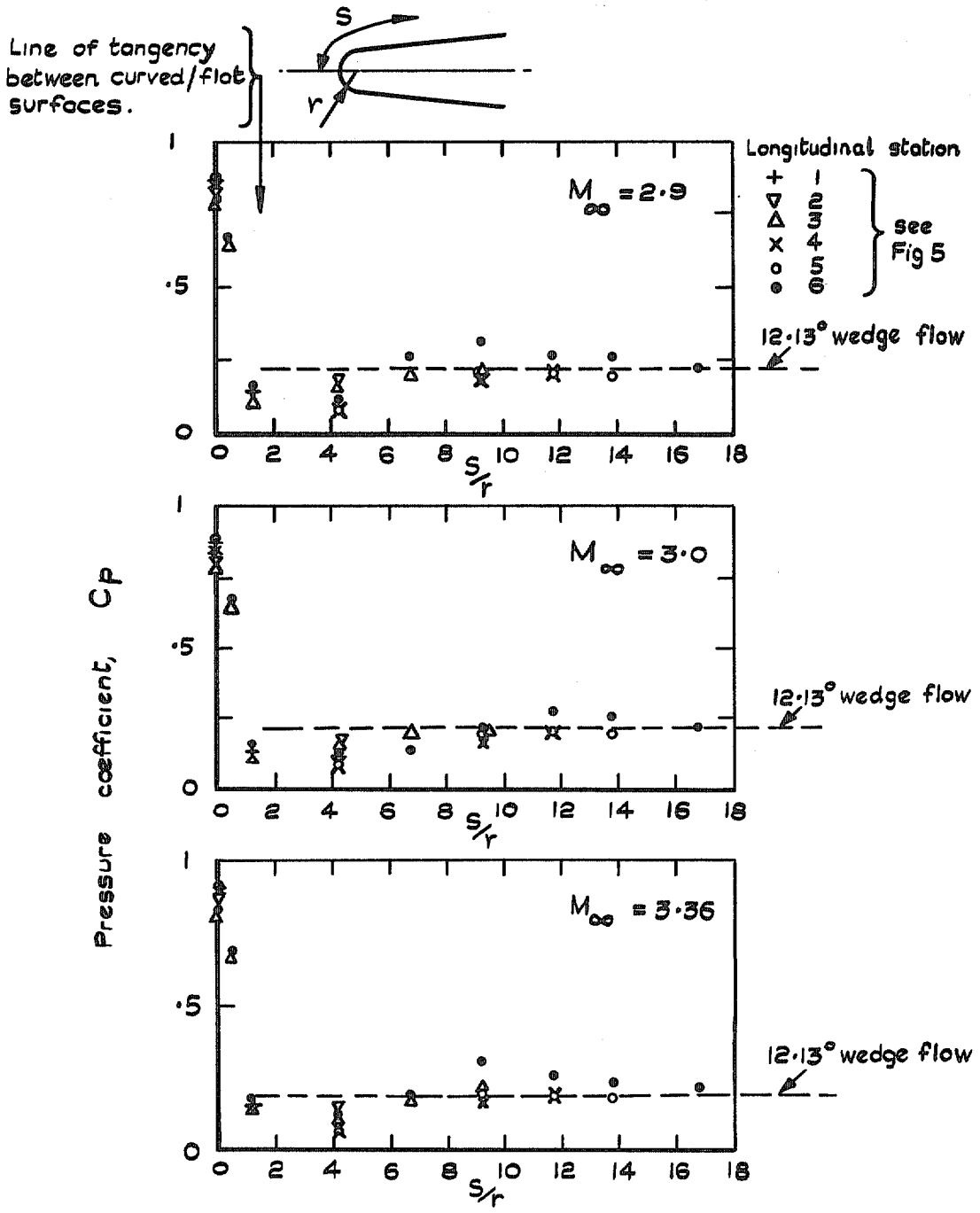

FIG. 14. Spanwise pressure distribution for M_∞ above design Mach number (i.e. $M_\infty > 2{\cdot}47$) (accelerating flight).

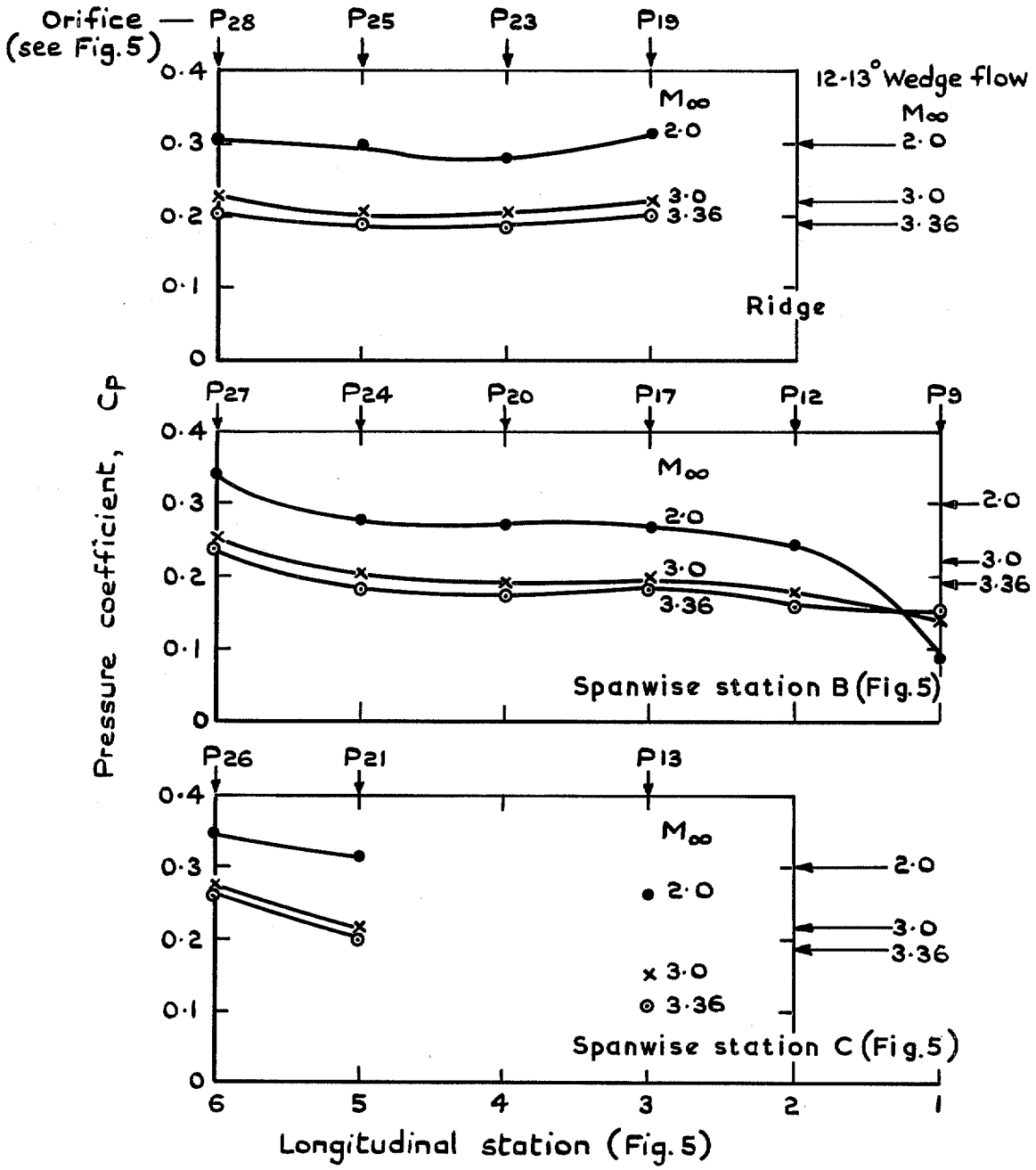

FIG. 15. Chordwise pressure distribution (accelerating flight).

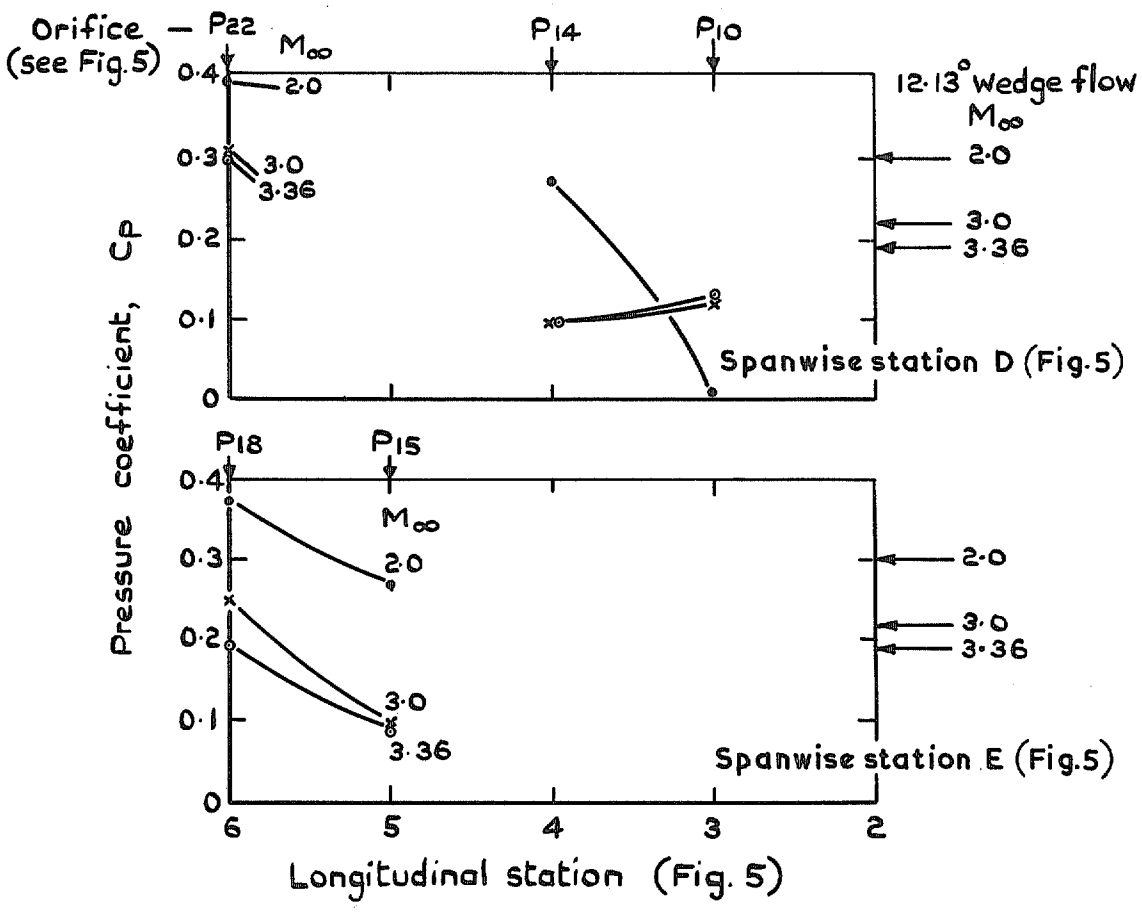

FIG. 15. (contd.) Chordwise pressure distribution (accelerating flight).

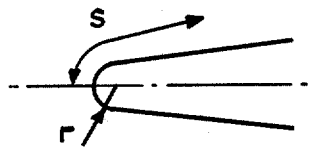

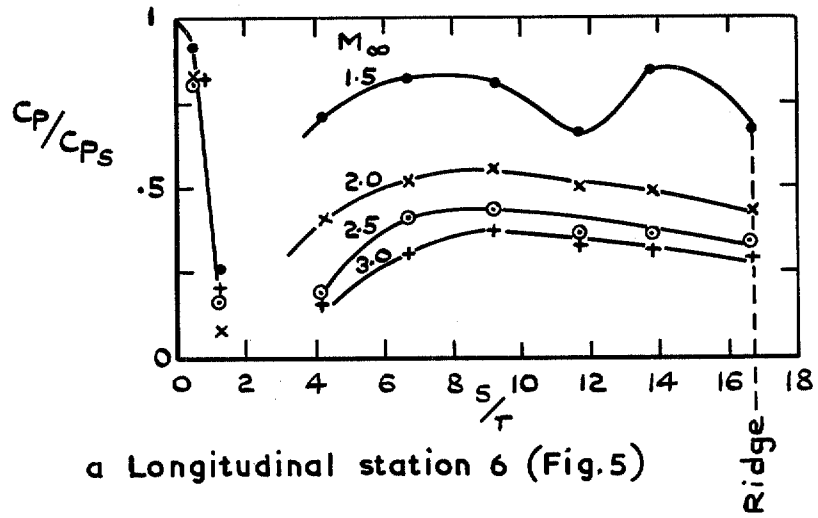

a Longitudinal station 6 (Fig.5)

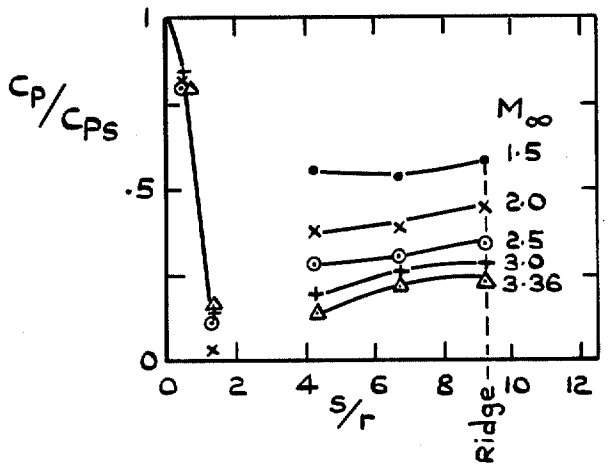

b Longitudinal station 3 (Fig.5)

FIG. 16 a & b. Spanwise pressure distribution as a fraction of leading-edge nominal stagnation pressure (C_{ps}) at two longitudinal stations (accelerating flight).

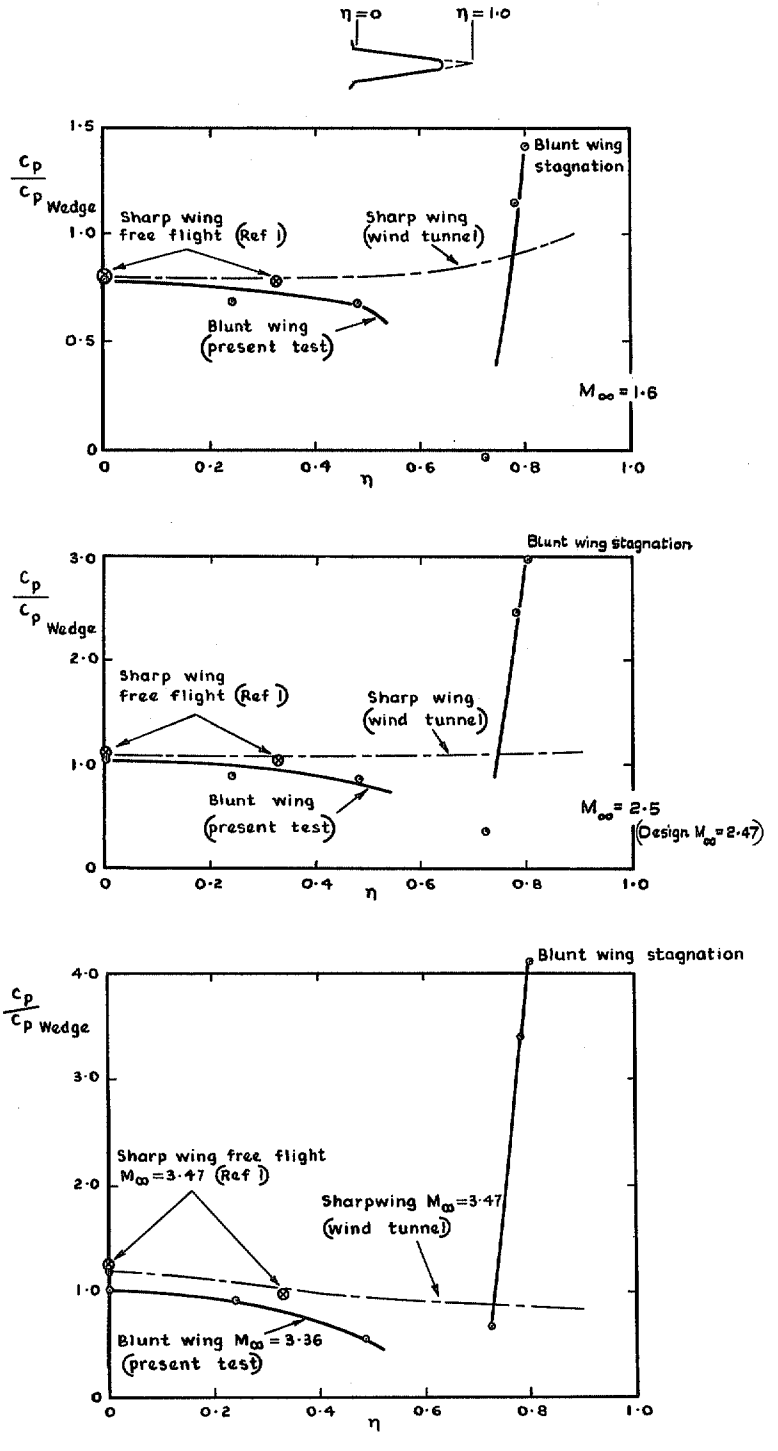

FIG. 17. Sharp/blunt wing comparison of spanwise pressure distribution—blunt wing data from longitudinal station 3 (Fig. 5) (accelerating flight).

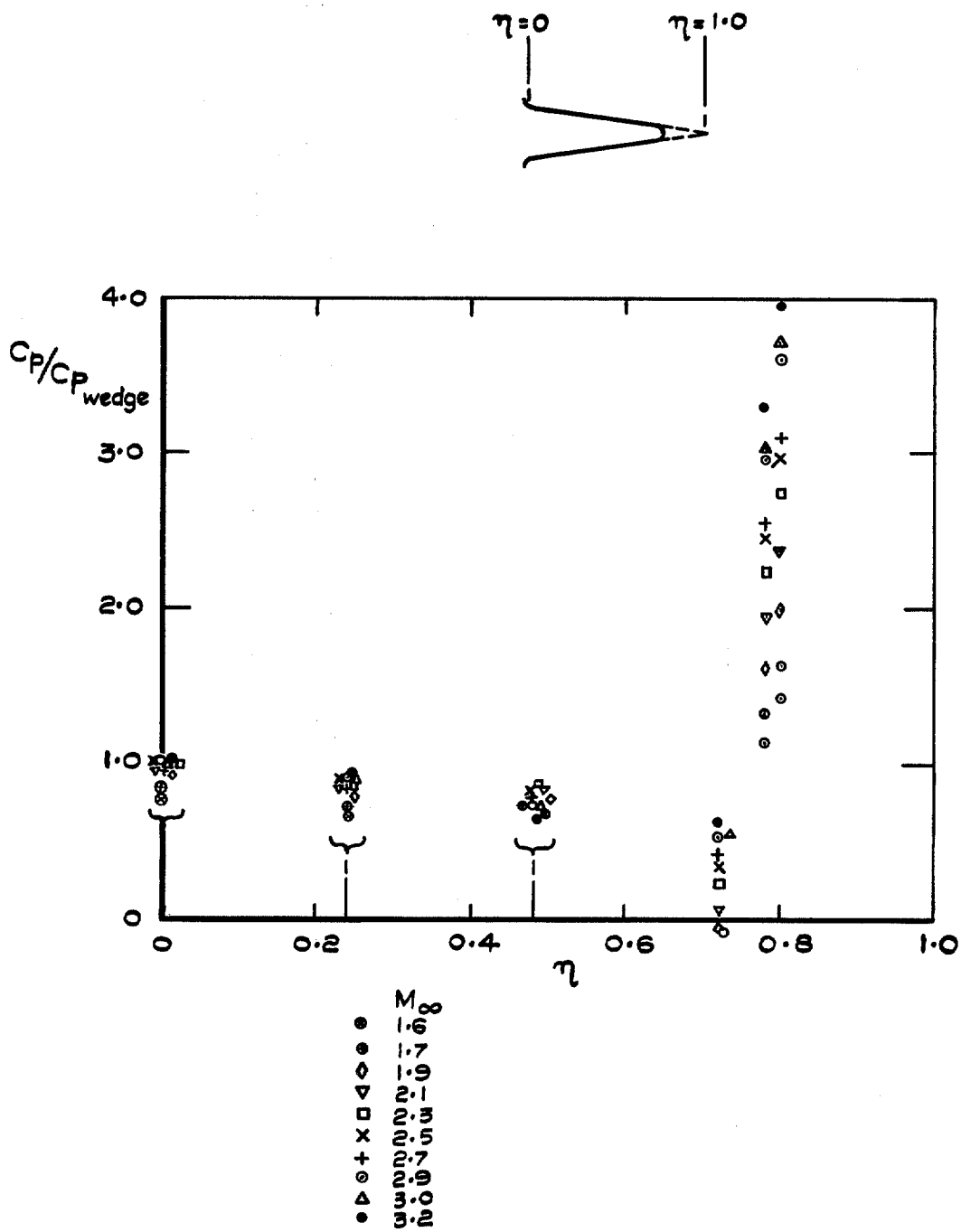

FIG. 18. Spanwise pressure distribution at longitudinal station 3 (blunt wing, present test).

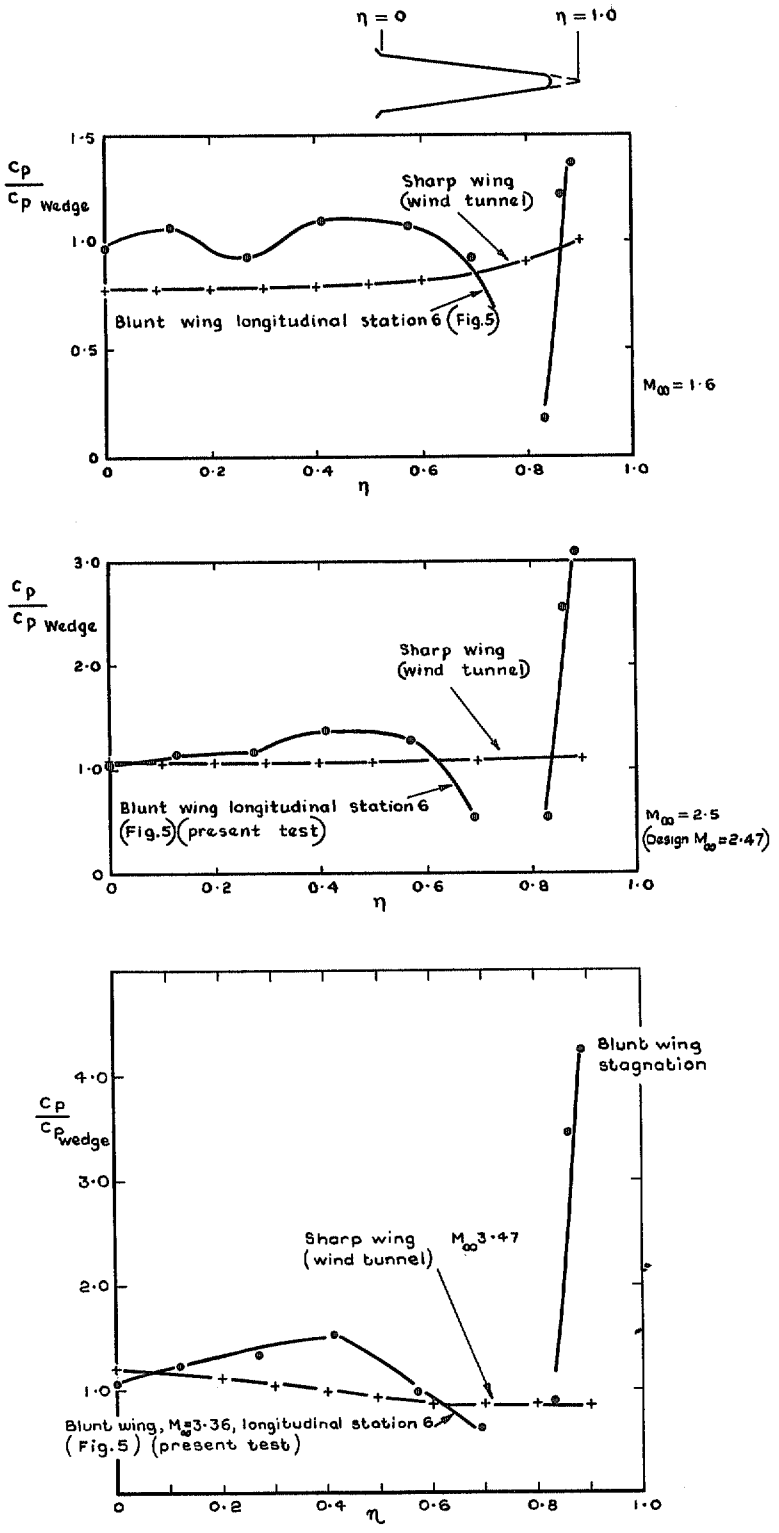

FIG. 19. Sharp/blunt wing comparison of spanwise pressure distribution—blunt wing data from longitudinal station 6 (Fig. 5) (accelerating flight).

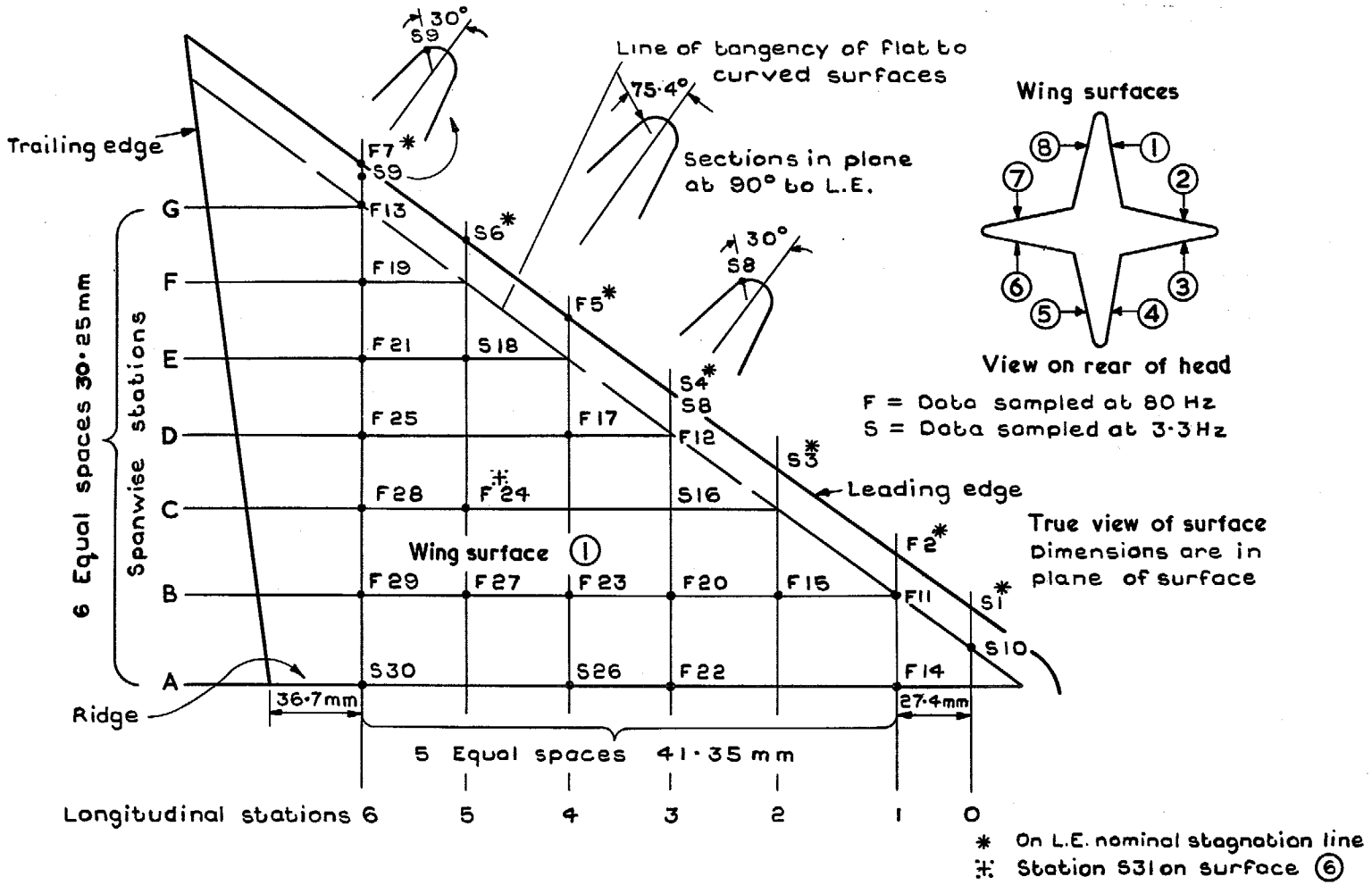

FIG. 20. Thermocouple locations.

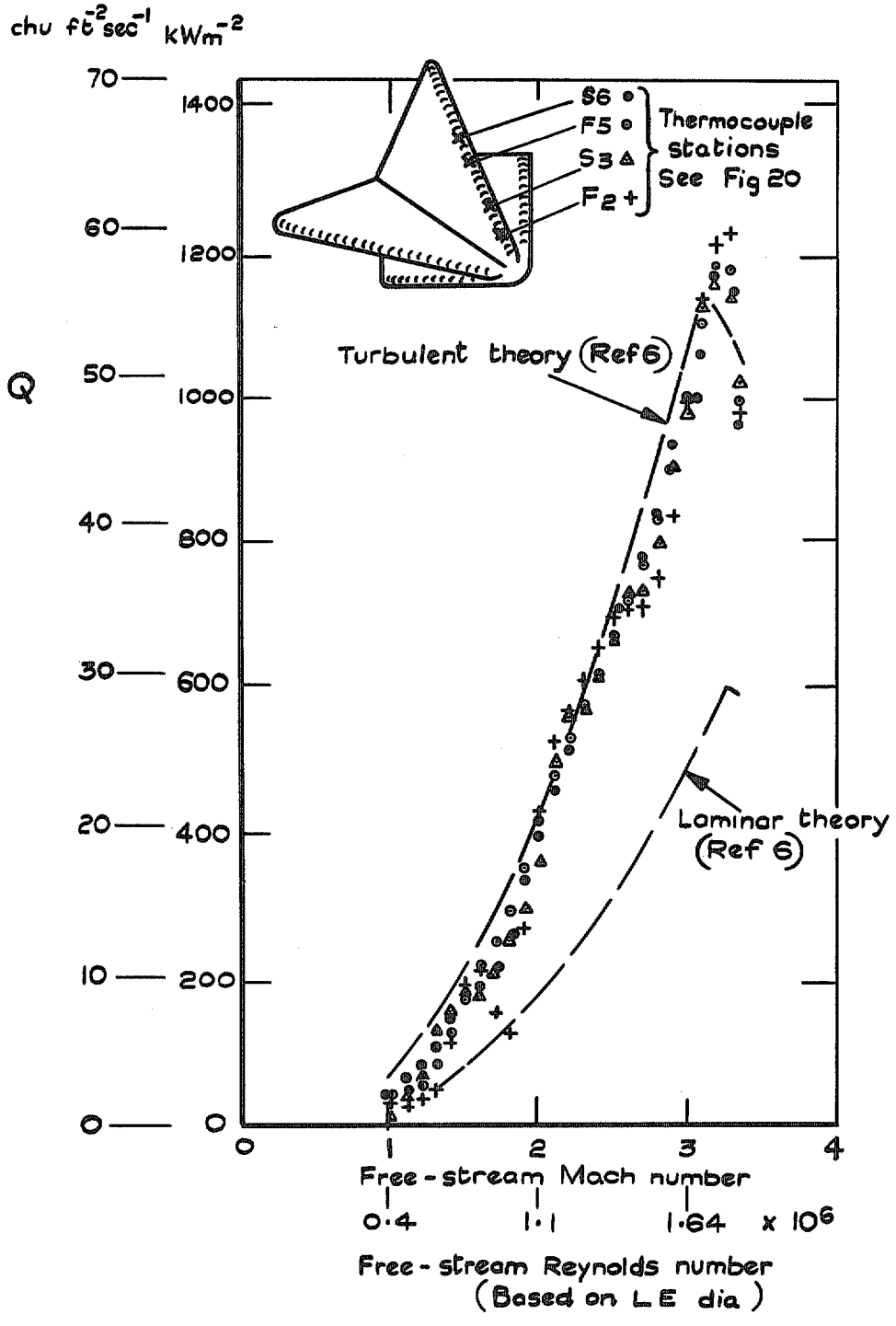

FIG. 21. Heat transfer to leading-edge nominal stagnation line accelerating flight.

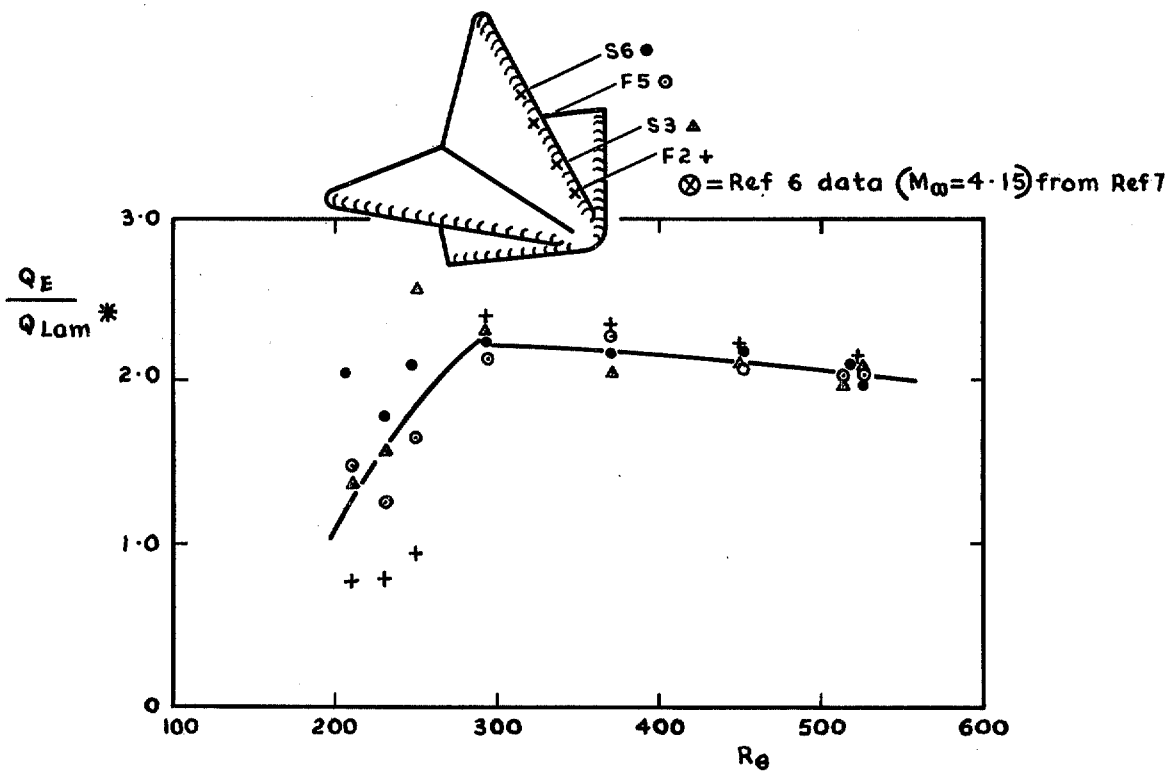

FIG. 22 a & b. Correlation of leading-edge stagnation heat flow with Reynolds number based on the spanwise momentum thickness of the stagnation line boundary layer (R_θ).

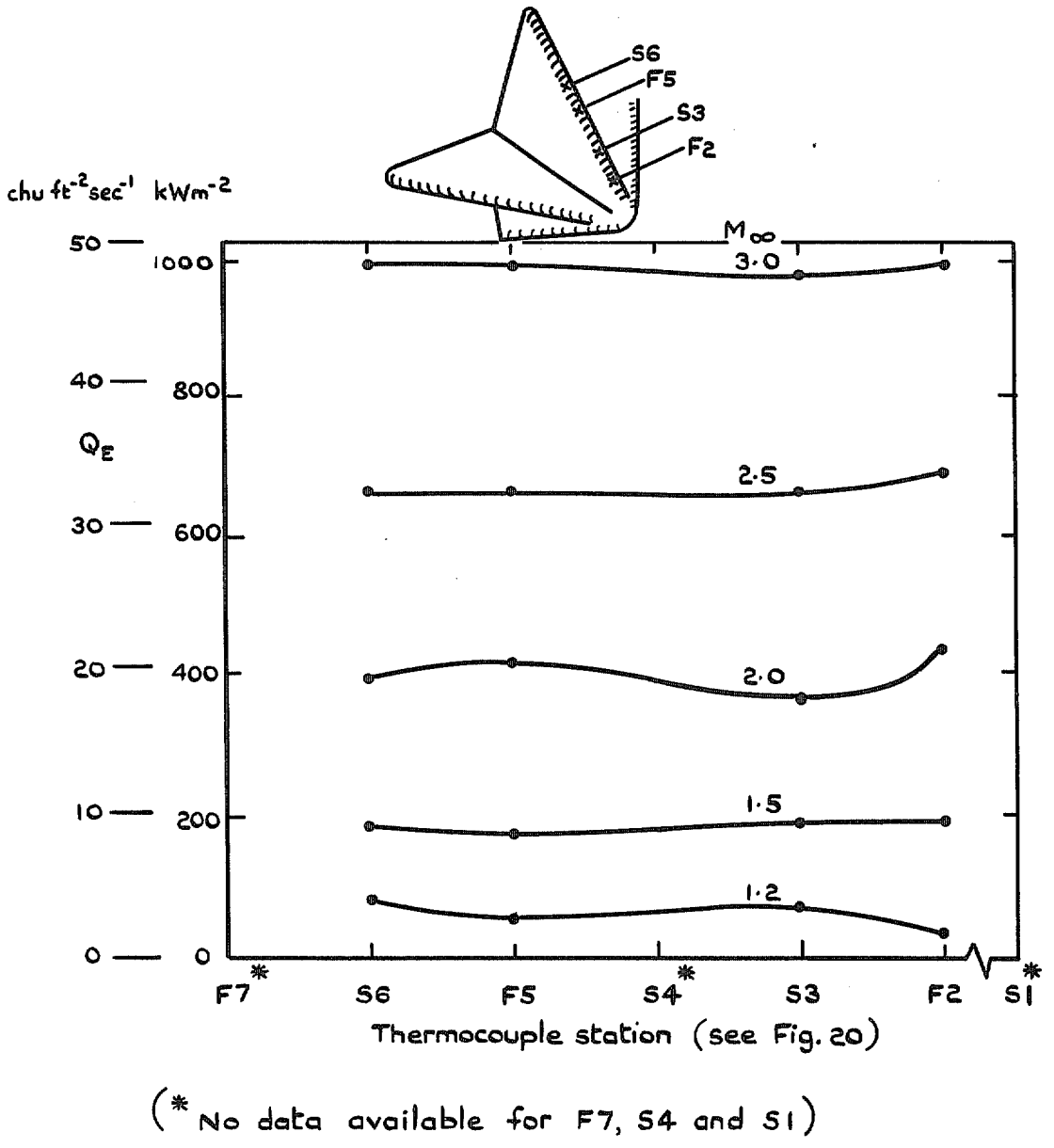

FIG. 23. Variation of heat transfer along leading-edge nominal stagnation line (accelerating flight).

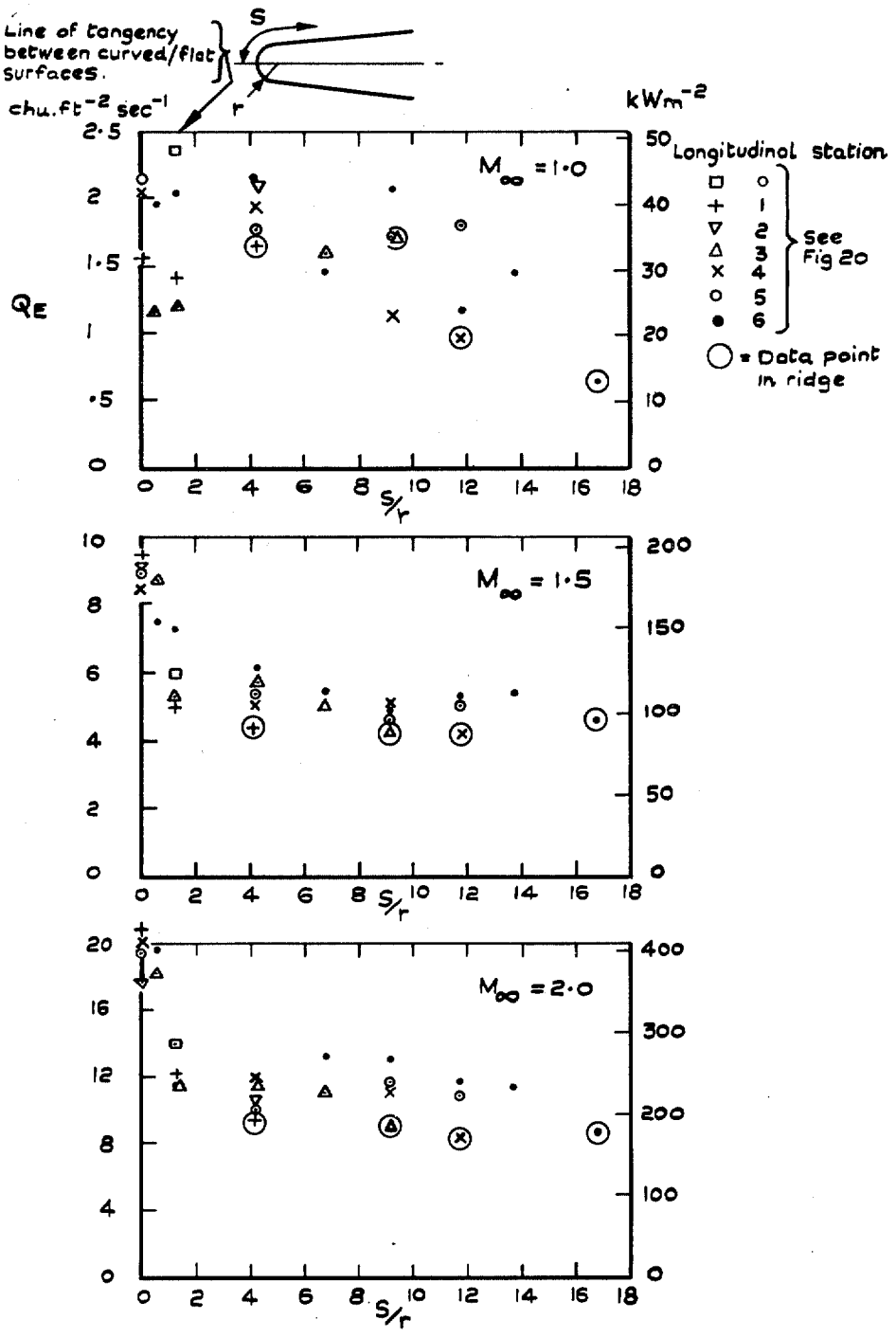

FIG. 24. Spanwise distribution of heat transfer for M_∞ below design Mach number (i.e. $M_\infty < 2{\cdot}47$) (accelerating flight).

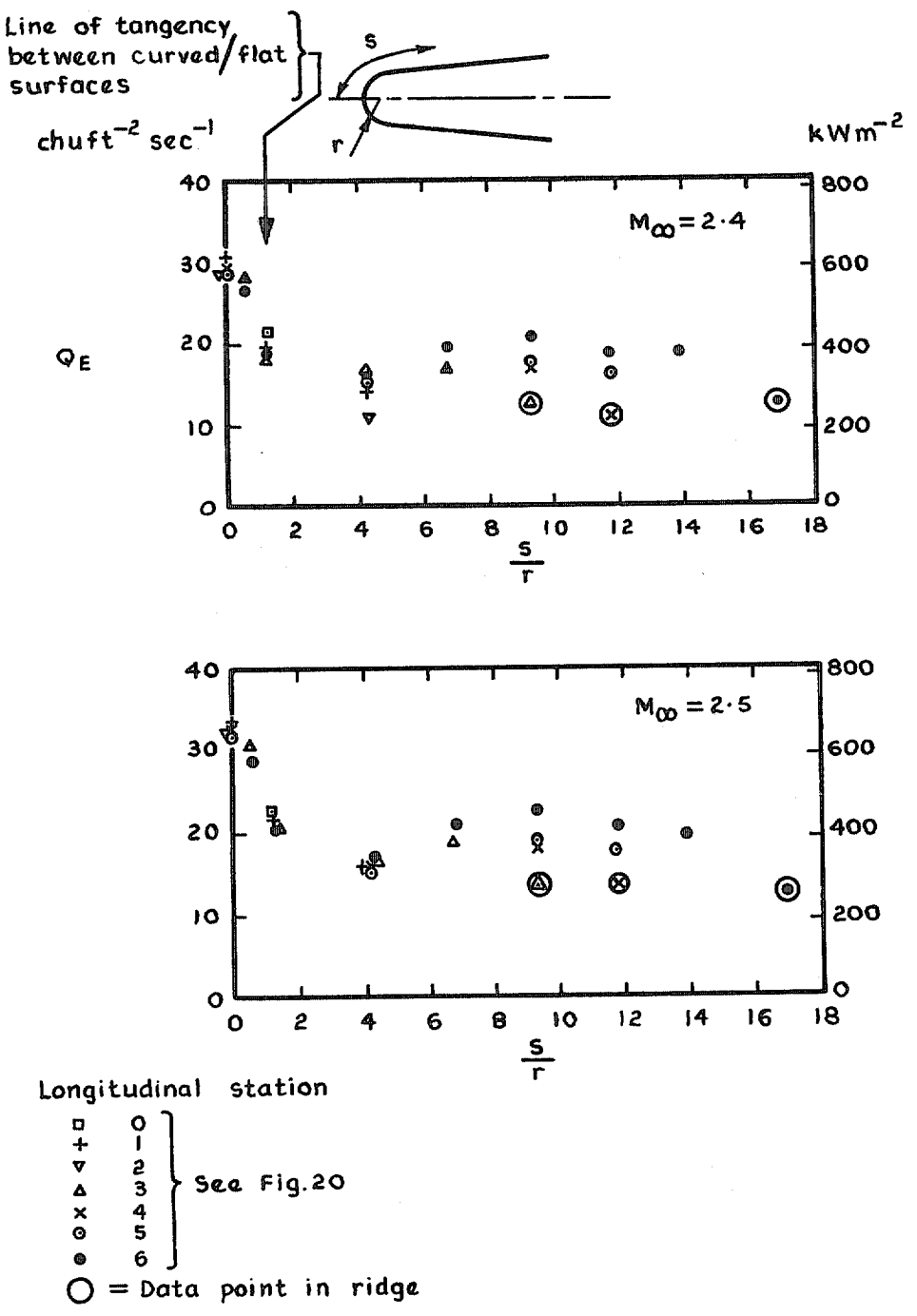

FIG. 25. Spanwise distribution of heat transfer for M_∞ near design Mach number (i.e. $M_\infty \approx 2{\cdot}47$) (accelerating flight).

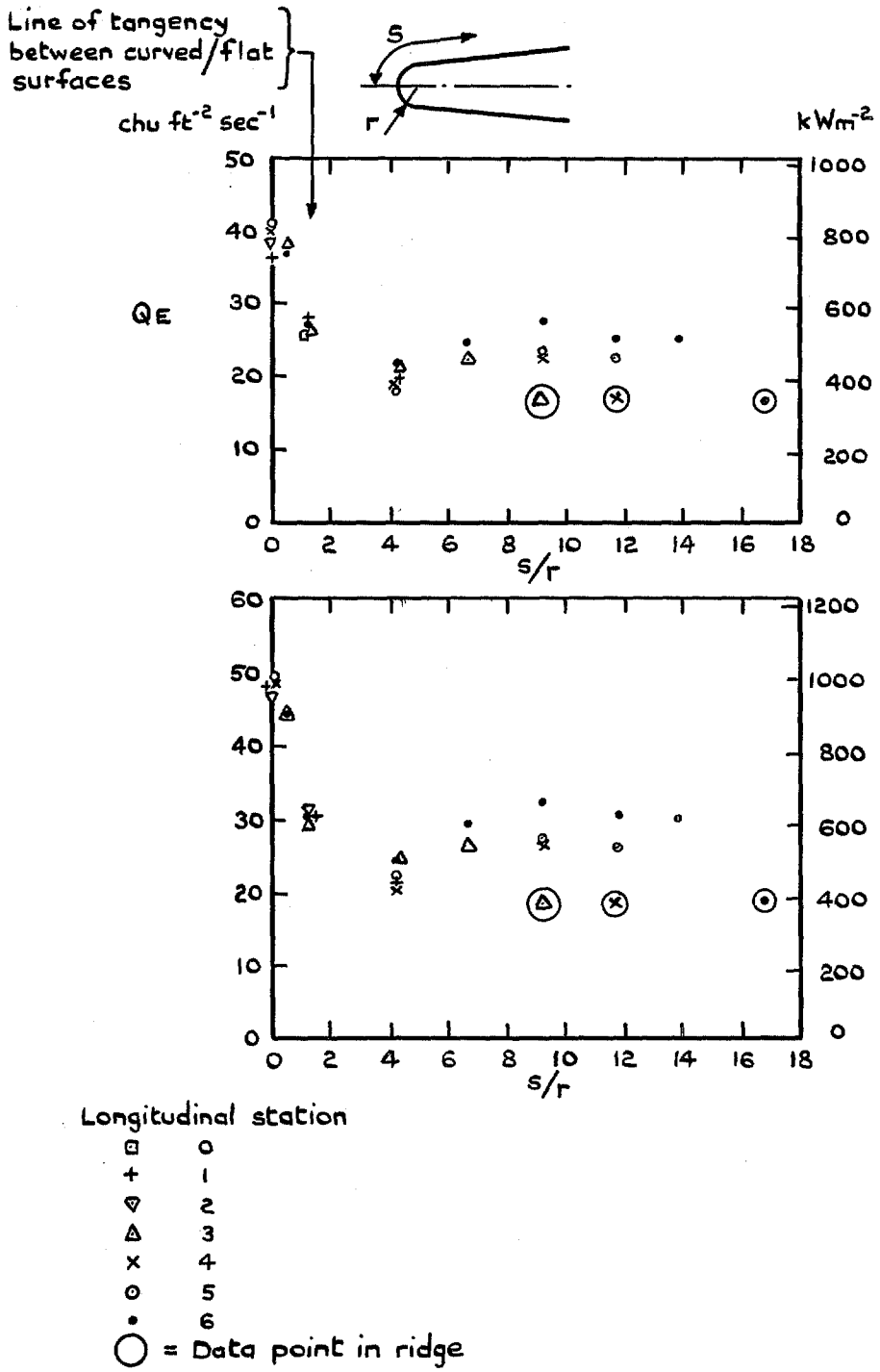

FIG. 26. Spanwise distribution of heat transfer for M_∞ above design Mach number (i.e. $M_\infty > 2{\cdot}47$).

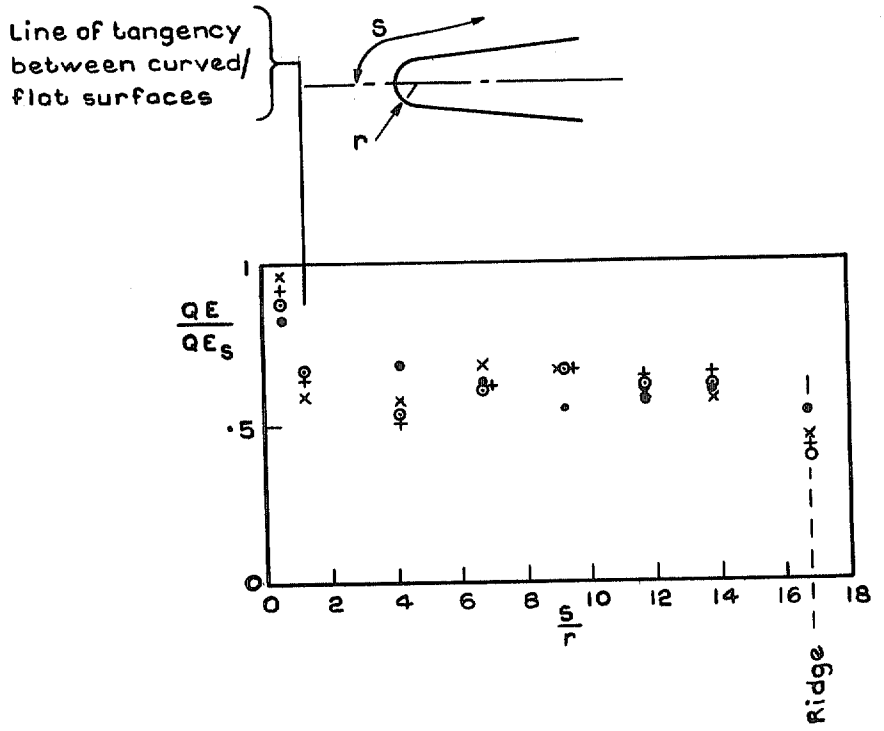

a Longitudinal station 6 (see Fig.20)

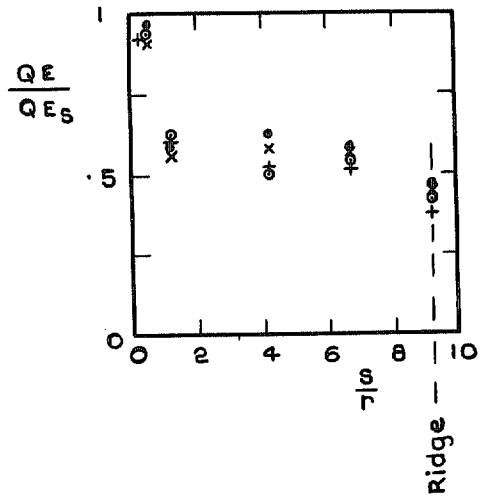

Key:

M_∞	
1·5	•
2·0	×
2·5	⊙
3·0	+

QE = Measured heat transfer to surface
QES = Measured heat transfer to wing leading edge stagnation point

b Longitudinal station 3 (see Fig.20)

FIG. 27. Spanwise heat transfer as fraction of leading-edge nominal stagnation heat transfer.

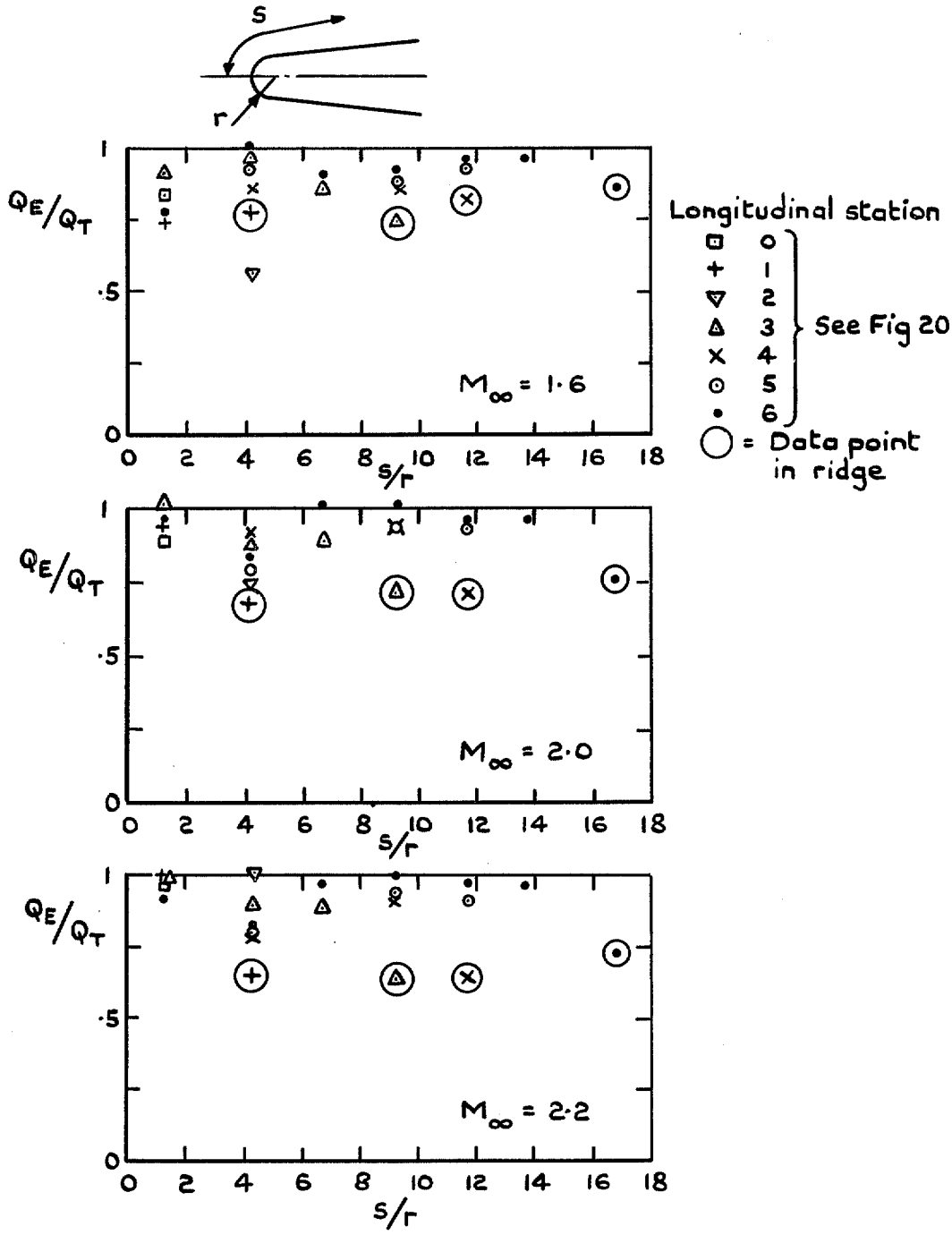

FIG. 28. Comparison of measured and estimated (turbulent) heat transfer to flat surface of wing for M_α below design Mach number (i.e. $M_\infty < 2{\cdot}47$) (accelerating flight).

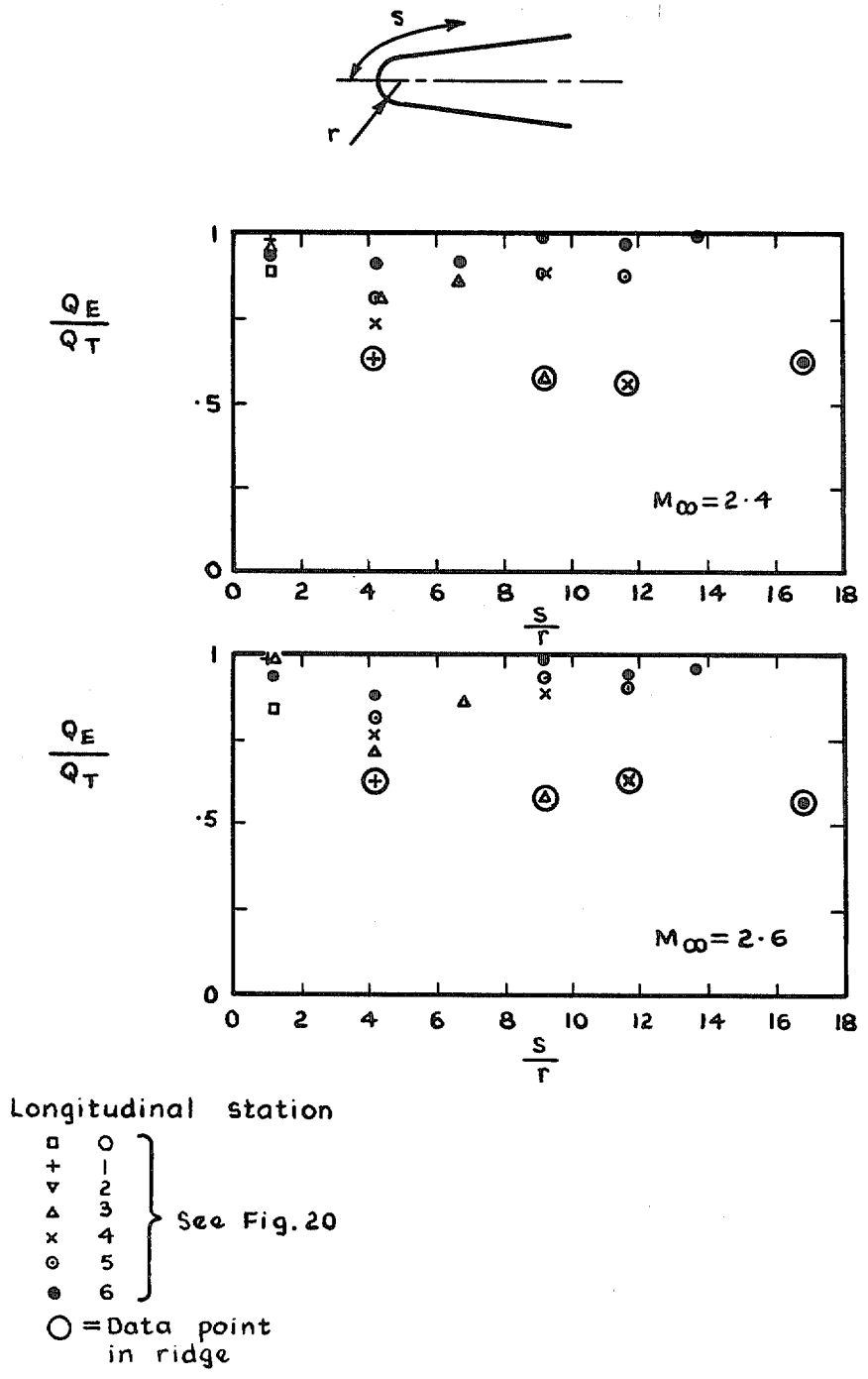

FIG. 29. Comparison of measured and estimated (turbulent) heat transfer to flat surface of wing for M_∞ near design Mach number (i.e. $M_\infty \approx 2{\cdot}47$).

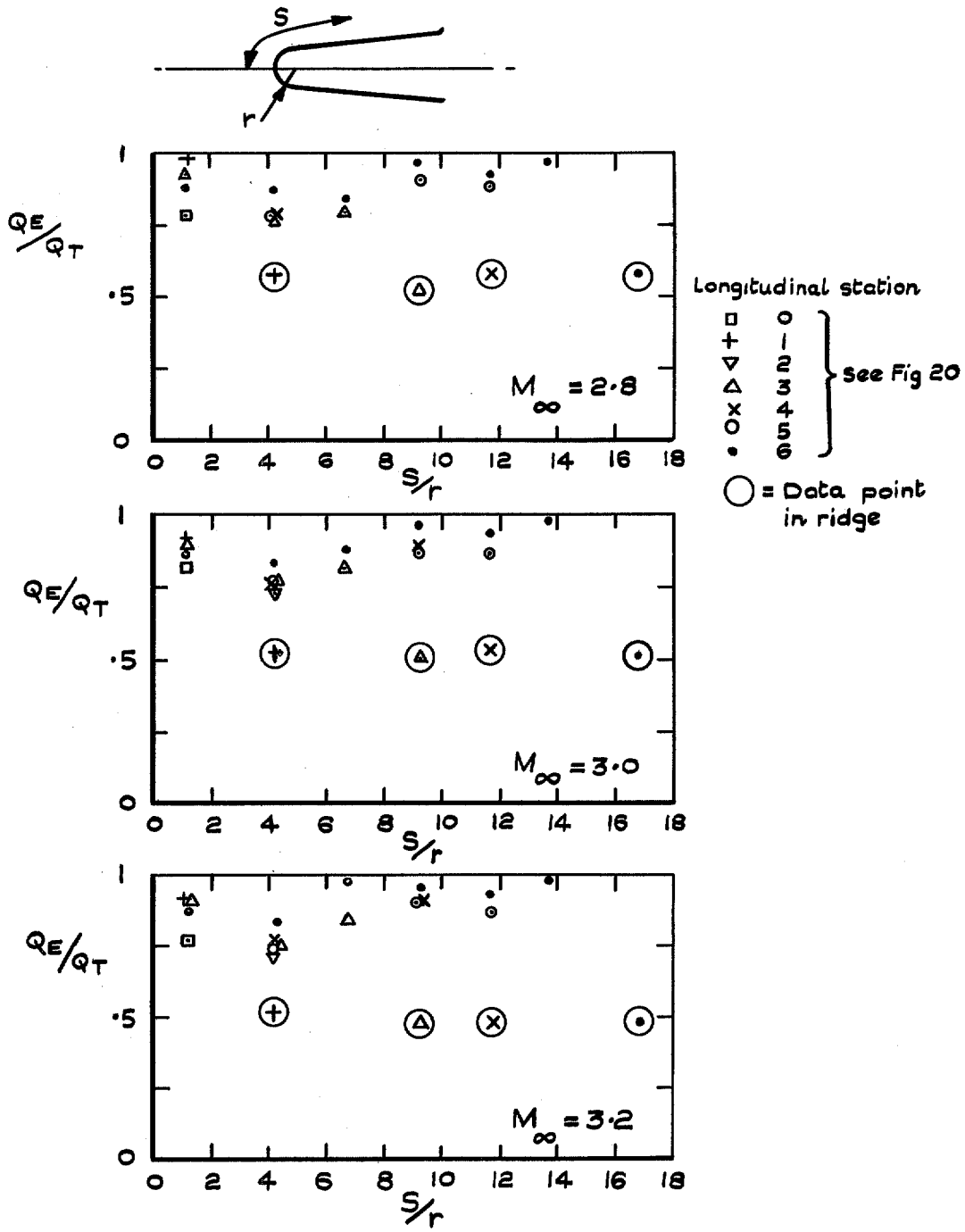

FIG. 30. Comparison of measured and estimated (turbulent) heat transfer to flat surface of wing for M_∞ above design Mach number (i.e. $M_\infty > 2{\cdot}47$).

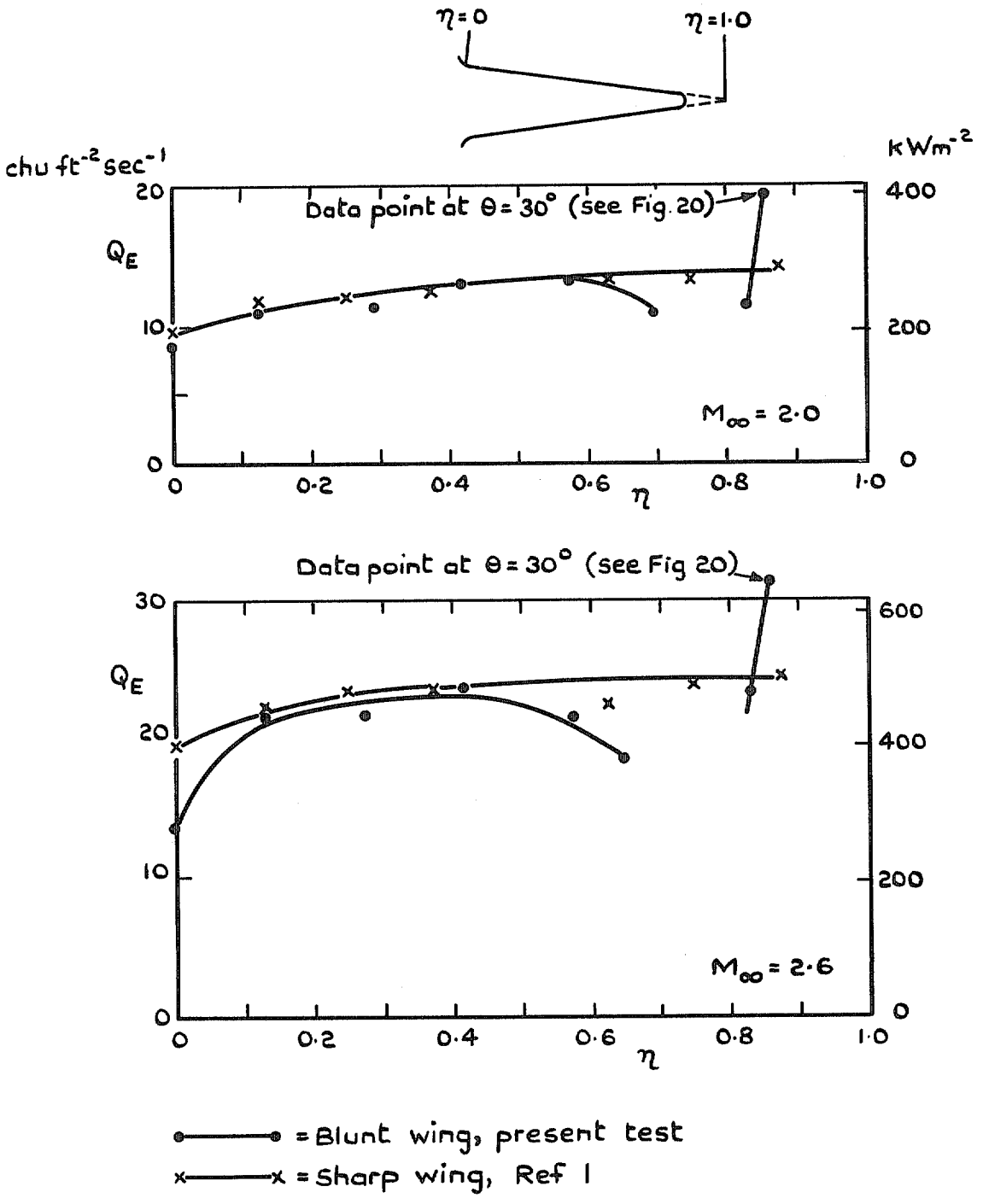

FIG. 31. Sharp/blunt wing comparison of spanwise heat-transfer rate—data for both wings from longitudinal station 6 (Fig. 20).

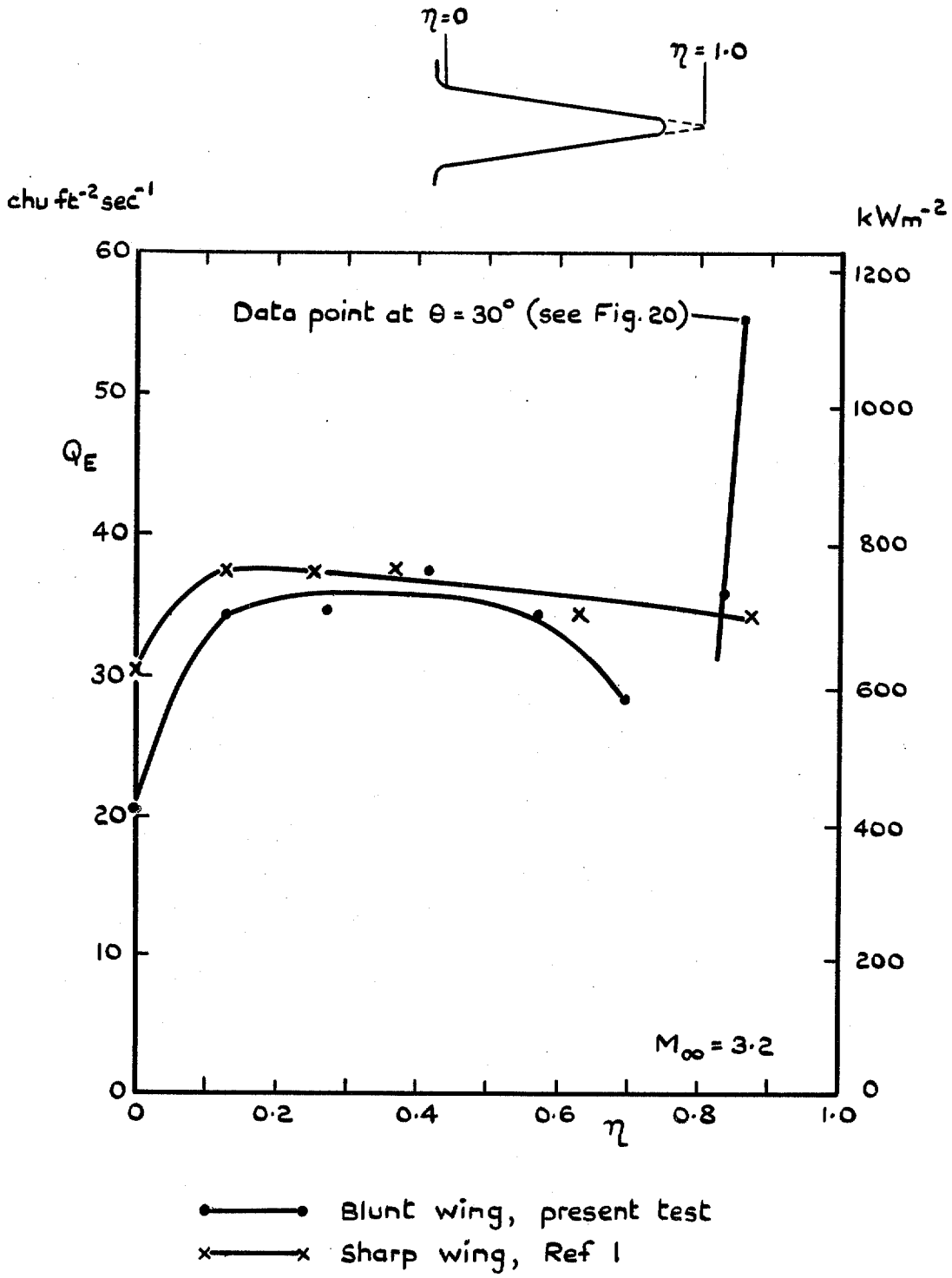

FIG. 31 (contd.) Sharp/blunt wing comparison of spanwise heat-transfer rate—data for both wings from longitudinal station 6 (Fig. 20).

Printed in Wales for Her Majesty's Stationery Office by Allens Printers (Wales) Limited

Dd. 502110 K.5. 10/71.

Published by
HER MAJESTY'S STATIONERY OFFICE

To be purchased from
49 High Holborn, London WC1V 6HB
13a Castle Street, Edinburgh EH2 3AR
109 St Mary Street, Cardiff CF1 1JW
Brazennose Street, Manchester M60 8AS
50 Fairfax Street, Bristol BS1 3DE
258 Broad Street, Birmingham B1 2HE
80 Chichester Street, Belfast BT1 4JY
or through booksellers

R. & M. No. 3679
SBN 11 470419 8